### **Supplementary information**

# Imaging viscous flow of the Dirac fluid in graphene

In the format provided by the authors and unedited

Mark J. H. Ku, Tony X. Zhou, Qing Li, Young J. Shin, Jing K. Shi, Claire Burch, Laurel E. Anderson, Andrew T. Pierce, Yonglong Xie, Assaf Hamo, Uri Vool, Huiliang Zhang, Francesco Casola, Takashi Taniguchi, Kenji Watanabe, Michael M. Fogler, Philip Kim, Amir Yacoby  $^{\bowtie}$  & Ronald L. Walsworth  $^{\bowtie}$ 

## **Supplementary Information for Imaging Viscous Flow of the Dirac Fluid in Graphene**

Mark J.H. Ku, Tony X. Zhou, Qing Li, Young J. Shin, Jing K. Shi, Claire Burch, Laurel E. Anderson, Andrew T. Pierce, Yonglong Xie, Assaf Hamo, Uri Vool, Huiliang Zhang, Francesco Casola, Takashi Taniguchi, Kenji Watanabe, Michael M. Fogler, Philip Kim, Amir Yacoby, and Ronald L. Walsworth

#### 1 Validity of mapping current density via magnetic field imaging

In the case of a static 2D current distribution  $\mathbf{J}(x,y) = (J_x(x,y), J_y(x,y))$ , there is a one-to-one mapping between  $\mathbf{J}(x,y)$  and the associated stray magnetic field

 $\mathbf{B}(\mathbf{r}) = (B_x(x,y,z), B_y(x,y,z), B_z(x,y,z))$ . Therefore, in principle one can equate the knowledge of the magnetic field distribution to the knowledge of the current distribution. Here, we evaluate several experimental factors that may invalidate this equivalence. We show that in our experimental setting, these factors are insignificant within experimental uncertainties, and hence it is valid to extract the local current density via magnetic field imaging.

First, we discuss the potential consequence of measuring  $\mathbf{B}(\mathbf{r})$  over a finite field-of-view. According to the Biot-Savart law, the in-plane stray field at (x, y, d) is

$$B_x(x,y,d) = \frac{\mu_0}{4\pi} \int dx' dy' \frac{d}{[(x-x')^2 + (y-y')^2 + d^2]^{3/2}} J_y(x',y')$$
 (S1)

$$B_y(x,y,d) = -\frac{\mu_0}{4\pi} \int dx' dy' \frac{d}{[(x-x')^2 + (y-y')^2 + d^2]^{3/2}} J_x(x',y'), \qquad (S2)$$

where  $\mu_0$  is the vacuum permeability. In other words, the in-plane stray field can be considered as a convolutional filter  $(x^2 + y^2 + d^2)^{-3/2}$  with a resolution length-scale d applied on the local current density. As a result,  $B_x(x,y,d)$  and  $B_y(x,y,d)$  are only sensitive to the current density in the neighborhood of (x,y) extending on the order of  $\sim d$ . This is also apparent with the forms of the above equations in Fourier space<sup>1</sup>:

$$b_x(\mathbf{k}, d) = \frac{\mu_0}{2} e^{-d|\mathbf{k}|} j_y(\mathbf{k}), \qquad (S3)$$

$$b_y(\mathbf{k}, d) = -\frac{\mu_0}{2} e^{-d|\mathbf{k}|} j_x(\mathbf{k}), \qquad (S4)$$

where **k** is the wave-vector, and  $b_{x,y}$  ( $j_{x,y}$ ) is the Fourier transform of  $B_{x,y}$  ( $J_{x,y}$ ). Therefore,  $(B_x, B_y)$  is equivalent to  $(J_x, J_y)$  with a low-pass filter, and the current density can be obtained by inverting the low-pass filter on the stray-field (e.g., in the case of vectorial wide-field imaging).

Let us now consider the case where the measured stray field involves the out-of-plane stray field  $B_z$ , for example in scanning magnetometry. From the Biot-Savart law, one has

$$B_z(x,y,d) = \frac{\mu_0}{4\pi} \int dx' dy' \frac{(y-y')J_x(x',y') - (x-x')J_y(x',y')}{[(x-x')^2 + (y-y')^2 + d^2]^{3/2}}.$$
 (S5)

Here, the convolutional kernel has the form  $\sim r/(r^2+d^2)^{3/2}$ . Therefore,  $B_z$  is not simply a low-pass filter applied on the current density. This is also apparent with the form of the above equation in Fourier space<sup>1</sup>:

$$b_z(\mathbf{k}, d) = i \frac{\mu_0}{2} e^{-d|\mathbf{k}|} \left( \frac{k_y}{|\mathbf{k}|} j_x(\mathbf{k}) - \frac{k_x}{|\mathbf{k}|} j_y(\mathbf{k}) \right).$$
 (S6)

The form of the kernel in Eq. S5 indicates that  $B_z(x,y,d)$  is insensitive to the current density in the immediate neighborhood of (x,y), while contribution from further away has greater weight. As a consequence,  $B_z$  has a slow  $\sim 1/r$  decay far away from a current-carrying wire segment. Therefore, when attempting to extract the local current density from a measurement that contains  $B_z$ , one needs to consider the potential contribution from current outside of the field of view. This can happen when the current-carrying channel does not continue in a straight line indefinitely, but makes a turn. Let us consider how close the turning needs to occur from the point of measurement so the contribution from far-away wire becomes important compared to the measurement precision, typically  $\sim 5\%$  on the maximal value of the projective field for our experiments. Let us consider a channel initially along the y-direction, which changes direction to run along the

x-direction at a distance r away from the point of measurement. Using the expression of the field away from a thin current-carrying wire, one can estimate the contribution to  $B_z$  as  $\mu_0 I/(4\pi r)$ . There is an extra factor of 2 in the denominator because after the turn, we have a semi-infinite wire. We estimate the field magnitude at the point of measurement to be  $(\mu_0/2)(I/W)$ , with  $W=1~\mu\mathrm{m}$ . Then, the contribution due to  $B_z$  from the far-away wire is comparable to 5% of the total measured field when r is closer than  $3~\mu\mathrm{m}$ . In the devices measured with NV scanning magnetometry, turning of current paths occurs on length-scales significantly greater than this distance. Therefore, the effect of slowly-decaying  $B_z$  from far-away current does not invalidate our approach to use magnetometry to probe the local current profile.

The discussion so far centers around the magnetostatic case. In AC magnetometry, the natural assumption is to replace  $\mathbf{J}(x,y)$  and  $\mathbf{B}(x,y,d)$  with  $\mathbf{J}(x,y,t)$  and  $\mathbf{B}(x,y,d,t)$ . In general, this is not strictly true because of the delay in the propagation of the electromagnetic field; the generalized time-dependent formula for the stray magnetic field is given by Jefimenko's equations which incorporate retarded time. Here, we show that our experiment is in the magnetostatic regime. Let us consider the current being modulated at a frequency  $\omega$ . At a point of measurement, the stray field is sensitive to contributions from current over a length scale r given by the distance between the measurement point and the current source. Over this length scale, an electromagnetic field propagates to the point of measurement within a time  $\tau_{\text{prop}} \sim r/c$ , where c is the speed of light. We can assume the experiment is in the magnetostatic regime if this time is much faster than  $1/\omega$ . In the scanning magnetometry experiment, the scan range is no more than  $5\,\mu\text{m}$ , so  $r < 5\,\mu\text{m}$  and  $\tau_{\text{prop}} < 17\,\text{fs}$ . Therefore, magnetostatics can be safely assumed for

 $\omega/(2\pi) \ll 60 \, \mathrm{THz}$ , which is certainly the case in our experiment.

Lastly, in AC magnetometry, RC reactance can lead to a slow rise/fall in current modulation. To assess the effect of RC reactance, we consider the effective circuit shown in Fig. S1 under a step voltage modulation  $V(t) = V\Theta(t)$ , where  $\Theta(t)$  is the Heaviside step function. The resistor  $R_1$  corresponds to the resistance of the graphene device and is at most  $R_1 \approx 20 \,\mathrm{k}\Omega$  as measured with two-terminal transport measurement. The resistor  $R_2 = 50 \,\Omega$  corresponds to the terminal load resistance. The capacitor C comes from a combination of bond pads and BNC cables, and is estimated via geometry to be no more than  $1 \,\mathrm{nF}$ . Solution of the current through  $R_1$  is

$$I(t) = \frac{V}{R_1 + R_2} \left[ 1 + \frac{R_2}{R_1} \exp\left(-\frac{(R_1 + R_2)}{CR_1 R_2}t\right) \right].$$
 (S7)

The current initially overshoots before reaching the equilibrium (DC) value  $V/(R_1 + R_2)$ . The time scale  $CR_1R_2/(R_1 + R_2) \approx 0.05 \,\mu\mathrm{s}$  is much shorter than the typical modulation period of our experiments  $\gtrsim 10 \,\mu\mathrm{s}$ . Furthermore, the relative overshoot is  $R_2/R_1 \lesssim 1\%$ . Therefore, RC reactance has negligible effect in our AC measurements.

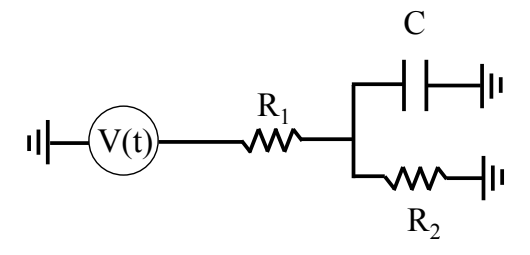


Figure S1: Effective circuit of the device.

#### 2 Optimal sensitivity for optically detected magnetic resonance

The best sensitivity for optically detected magnetic resonance (ODMR) is achieved by minimizing the ratio  $\Gamma/(\mathcal{C}\sqrt{\mathcal{N}})$ , where  $\Gamma$  is the linewidth of the ODMR spectrum,  $\mathcal{C}$  is the contrast, and  $\mathcal{N}$  is the rate of photon collection. In general, both the linewidth and the contrast depend on the combination of the optical and microwave power. In both imaging and scanning experiments, we are limited by the laser intensity that can be delivered to the NV spins: we restrict the excitation power to be below saturation to avoid NV degradation (likely due to charge state interconversion). In imaging, we are further restricted by the available laser power, which has to be distributed over a microns-scale area. Therefore, the only remaining knob is the microwave power. We obtain ODMR spectra, measure  $\Gamma$  and  $\mathcal{C}$  as a function of the microwave power, and use the microwave power that minimizes the ratio  $\Gamma/\mathcal{C}$  for ODMR. In the case of imaging, this procedure is performed with the ODMR spectra integrated over the entire field of view. In Fig. S2, we show an example spectrum at a single pixel of wide-field ODMR imaging of the graphene device on diamond at the optimal magnetometry parameters.

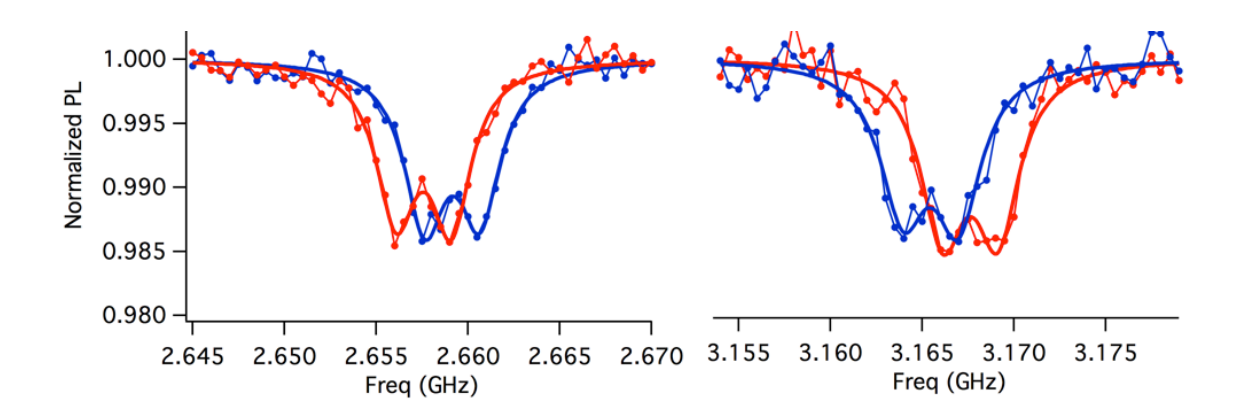


Figure S2: Wide-field imaging ODMR spectrum at a single pixel for the NV  $m_s=0 \leftrightarrow -1$  (left panel) and  $m_s=0 \leftrightarrow +1$  (right panel) transitions at +I (red circles) and -I (blue circles). Photoluminescence (PL) is normalized by the PL value of  $m_s=0$  state. The lines are fits to double Lorentzian line shapes split by 3 MHz hyperfine coupling due to  $^{15}$ N nuclear spin.

#### 3 Determination of magnification and resolution for wide-field imaging

For wide-field magnetic imaging, we calibrate magnification with the following procedure. Using the nano-positioner on which the graphene-on-diamond device is mounted, we move the device in the xy plane over a range of about  $7\,\mu\mathrm{m}$ , and record an image with each lateral movement of the nano-positioner. By tracking features in the image and using the known pixel size of the camera  $(5.86\,\mu\mathrm{m} \times 5.86\,\mu\mathrm{m})$ , we obtain a magnification of about 117. Therefore, each pixel on the camera corresponds to a 50 nm  $\times$  50 nm area on the sample. For data analysis and display, we perform a 2  $\times$  2 binning, so that each pixel in the figures corresponds to a 100 nm  $\times$  100 nm area. This calibration procedure has an estimated 6% error due to measurement uncertainty.

The point spread function (PSF) is given by the Airy pattern with the form

$$PSF_{Airy}(u) = \left(\frac{2J_1(u)}{u}\right)^2, \tag{S8}$$

where  $J_1$  is the Bessel function of the first kind of order one, and u is a dimensionless length scale. The first zero occurring at  $u=3.8317\approx 4$  corresponds to the resolution according to the Rayleigh criterion. For convenience, we use a Gaussian profile to approximate the PSF. The Airy pattern to leading order in u is  $\mathrm{PSF}_{\mathrm{Airy}}=1-u^2/4+\mathcal{O}(u^4)$ . A Gaussian profile of the form  $e^{-u^2/4}$  has the same expansion. Therefore, we use the following as our resolution function

$$PSF(x,y) = \frac{1}{\pi \sigma_{r}^{2}} e^{-(x^{2}+y^{2})/\sigma_{r}^{2}}$$
 (S9)

and identify  $2\sigma_{\rm r}$  as the imaging resolution.

To experimentally determine the resolution, we make use of a sharp feature in the NV PL

generated by reactive ion etching (RIE) of the diamond surface. As the RIE employed for graphene/hBN etching also etches diamond and hence near-surface NV spins, we can use RIE to generate patterns in the NV PL. The pattern we use is a stripe (Fig. S3a). We image a line cut (indicated by the blue line in Fig. S3a), normalize the slowly-varying background to unity, and show the normalized PL in Fig. S3b. To model the PL distribution, we first note the 1D PSF is  $PSF_{1D}(x) = \int dy \, PSF(x,y) = e^{-x^2/\sigma_r^2}/(\sqrt{\pi}\sigma_r)$ . The 1D line-cut of the stripe is then the convolution of the 1D PSF and the rectangular function  $\Pi(x/W)$ , which is unity for |x/W| < 0.5 and zero otherwise, with W the width of the stripe:

$$PSF_{1D} * \Pi(x/W) = \frac{1}{2} \left( Erf \left( \frac{W - 2x}{2\sigma_r} \right) + Erf \left( \frac{W + 2x}{2\sigma_r} \right) \right),$$
 (S10)

where  ${\rm Erf}(x)$  is the error function. From a fit of this form to the normalized PL line-cut (Fig. S3b), we obtain a resolution of  $2\sigma_{\rm r}=420(40)\,{\rm nm}$ . This is consistent with the estimated resolution assuming a PL wavelength  $\lambda$ =650 nm and NA=0.9:  $0.61\lambda/{\rm NA}=440\,{\rm nm}$ .

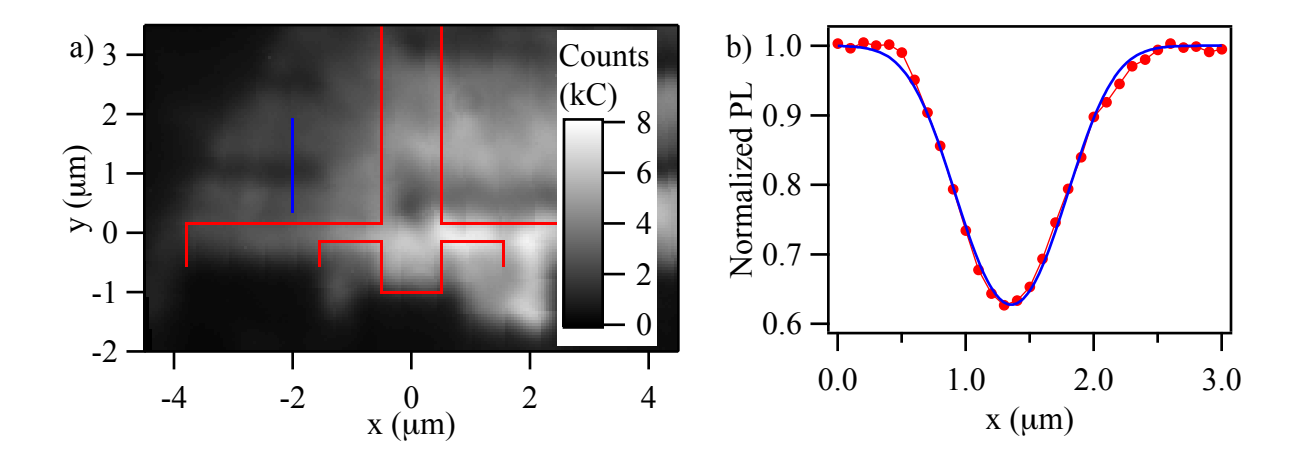


Figure S3: (a) NV photoluminescence (PL) image of the graphene-on-diamond device. The red outline indicates the boundary of the graphene channel. Some of the dark regions are due to shadows cast by metallic contacts, which include electrical contacts to the graphene channel and side probes, as well as top gate contacts. These PL features are not sharp due to the thickness of the metallic structures. Therefore, we use RIE to generate sharp features in NV PL, such as the stripe marked by the blue line. The blue line indicates the 1D line-cut used to generate the profile shown in (b), which we use to extract the resolution. We note that there is no PL feature corresponding to the outline of the graphene, because we did not etch all the way through the bottom hBN when patterning the hBN-encapsulated graphene heterostructure. However, for generating the stripe, we etched longer in order to etch through the hBN and hence remove the NV spins underneath. (b) Normalized PL line-cut measurements (red circles). Here, we normalize the slowly-varying background to unity. Hence, the depletion of the stripe feature has a relative contrast of about 40% with respect to the background. We fit the normalized PL to Eq. S10 (blue) to extract the resolution.

#### 4 Pulse sequence for spin-echo AC magnetometry

In Fig. S4, we show the pulse sequence for spin-echo AC magnetometry. The NV spin is first optically polarized into the  $m_s=0$  level. A  $(\pi/2)_x$  microwave pulse resonant with the  $m_s=0$   $\leftrightarrow -1$  transition creates a coherent superposition between these two states. The system evolves for a period of time  $\tau$  in the presence of a field  $B_{\rm AC}$  generated by a bias  $V_{\rm AC}$  applied on the device, and after a  $(\pi)_x$  refocusing pulse evolves for another  $\tau$  in the presence of  $-B_{\rm AC}$  generated by  $-V_{\rm AC}$ . For read-out, the electronic spin state is projected onto the  $m_s=0$ , -1 basis by a final  $\pm (\pi/2)_{x,y}$  pulse, and the ground state population is detected optically via spin-dependent fluorescence. Here,  $(\dots)_i$  refers to a rotation of the Bloch vector around  $S_i$  axis, where  $(S_x, S_y, S_z)$  are the spin operators.

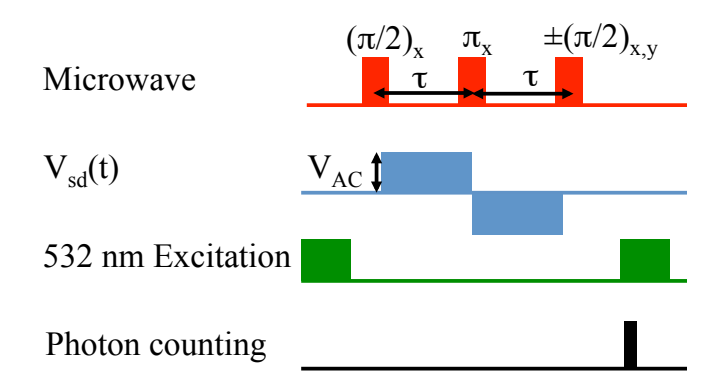


Figure S4: Pulse sequence for spin-echo AC magnetometry.

## 5 Current reconstruction for scanning probe magnetometry applied on simulated current profiles

To show the fidelity of the current reconstruction algorithm for scanning magnetometry, we test the algorithm on simulated current profiles. In Fig. S5, we show a simulation with three different types of current profiles: a uniform profile, a uniform profile with two bumps, and a parabola with two bumps. The total current, width, and noise level are chosen to be comparable to those in the experiment with graphene devices. The simulated data for  $B_{||}$  has a noise of 5% on the maximal  $B_{||}$ . As shown here, the reconstructed current profile is typically within 5% of the original current profile. For the simulation of a uniform current, while the reconstructed current occasionally deviates beyond 5% from the original profile, the standard error of the mean is 6%.

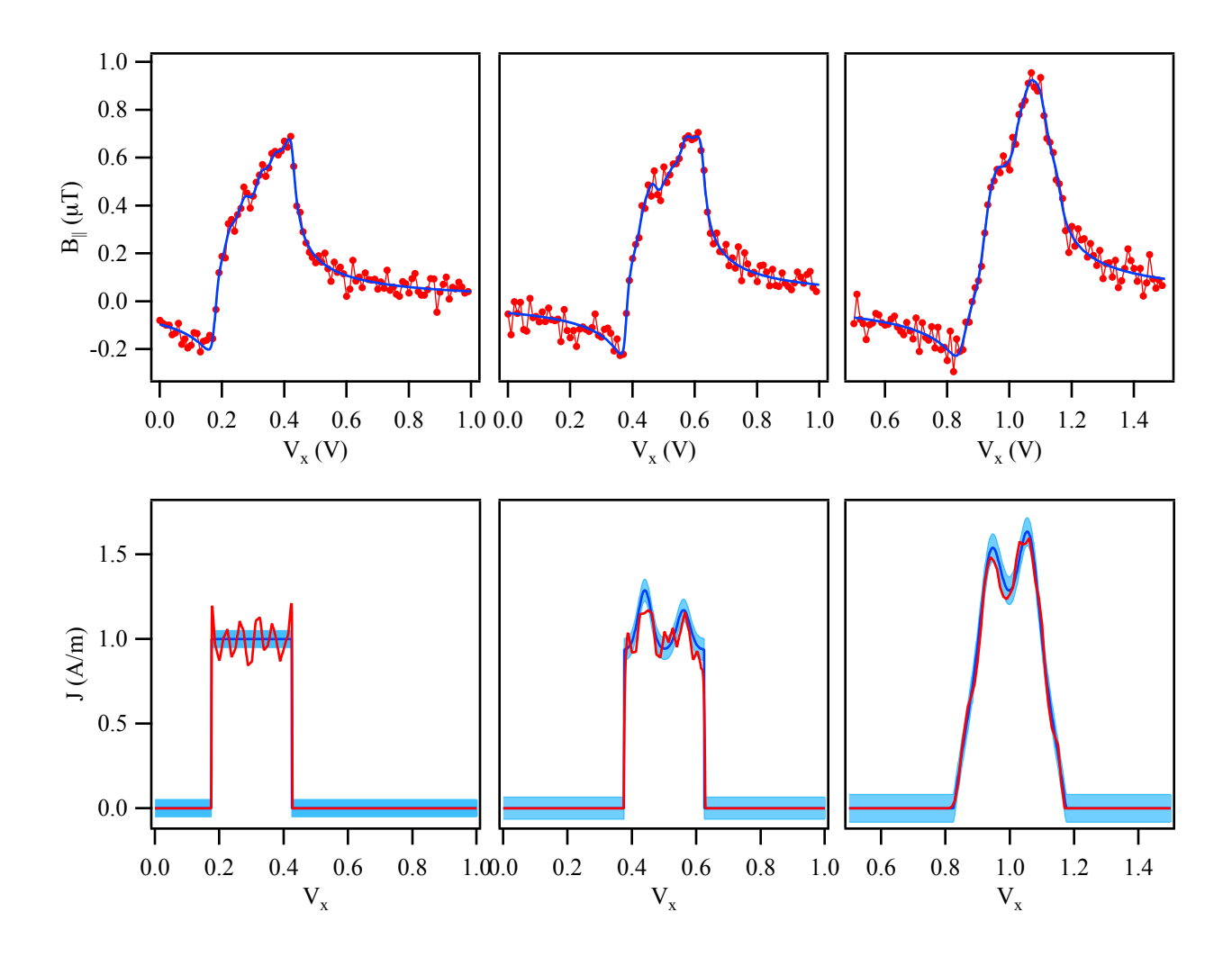


Figure S5: Current reconstruction applied to simulated profiles. Left to right: simulation is performed on three different current distributions: (left) a uniform distribution, (middle) a uniform distribution with two bumps, and (right) a parabola with two bumps. The x-axis is shown in units of the piezo scanning voltage. All profiles have  $I=1\,\mu\mathrm{A}$ . Top: simulated data for the projected field (red points) along with  $B_{||}$  generated from the reconstructed current profile (blue curves). Simulated data has 5% noise on the maximal value of the field. Bottom: result of reconstructed current profile (red) compared to the original (dark blue curve). The light blue band is the 5% error band for assessing the goodness of the reconstruction.

#### 6 Sensitivity of current reconstruction to uncertainty in the stand-off distance

NV centers used in this work are generated with nitrogen ion implantation at 6 keV. Stopping and Range of Ions in Matter (SRIM) calculation gives an estimate of 10(3) nm for the depth of the nitrogen, with the error bar denoting the ion straggle. However, experiments from Refs.  $^{2,3}$  indicate that the actual average NV depth for such shallow implants may be up to a factor of two larger compared to the estimate from SRIM. Therefore, for the NV spin ensemble in the wide-field imaging measurement, we estimate an average depth of 20 nm with uncertainty of 10 nm, which includes both the uncertainty of the average of the distribution as well as the straggle. The bottom hBN has a thickness close to 30 nm. Therefore, we use d=50(10) nm for the current reconstruction. The uncertainty in the stand-off distance leads to an 9 A/m (or 6%) error on the current density.

For the single NV scanning measurement, the stand-off distance d is one of the free parameters in the Biot-Savart functional and therefore is extracted. The extracted d has some distribution and can vary over a range up to 50 nm. On average, the extracted d is below 60 nm, which is consistent with the experimental setup:  $\approx 20(10)\,\mathrm{nm}$  from the 6 keV implant plus the thickness of the top hBN ( $\lesssim 20\,\mathrm{nm}$ ) or the finite thickness of the Pd wire ( $\approx 30\,\mathrm{nm}$ ). Given that a variation of d over  $\sim 10\,\mathrm{nm}$  scale is not expected to change the generated stray field much, we do not expect to be able to extract d to high precision. This is reflected in the uncertainty of d which is generally around 20 nm to 40 nm. We can evaluate the effect of the spread of d by extracting the current profile when we fix d to a specific value. Fig. S6 displays variation in the

reconstructed current profiles of a Pd channel and an encapsulated graphene device shown in Fig. 2e of the main text, corresponding to d fixed at several values. Here, the range of variation in d corresponds to the typical spread of the extracted d. For the Pd wire, with  $\pm 15\%$  change in d, we see a 2%-7% change in the current profile; whereas with the same variation in d, even less change in the current profile is observed for graphene. The typical error on the current density estimated here is consistent with  $\approx 5\%$  error assessed from simulated current profiles.

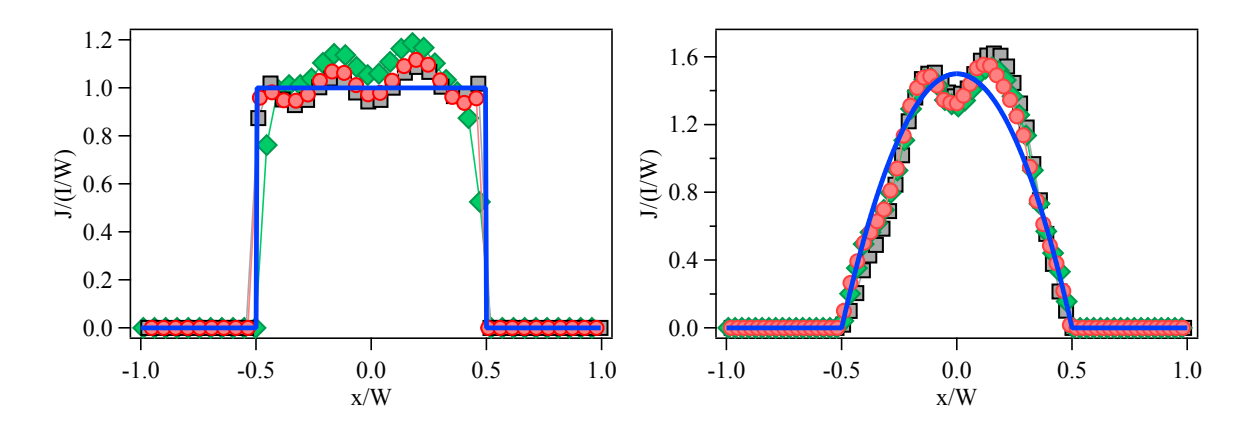


Figure S6: Variation in current profiles in Fig. 2e of the main text at various values of d. Red: allowing d to be extracted from the current reconstruction algorithm. Extracted d is 60(10) nm for the Pd channel (left panel) and 20(20) nm for the graphene device (right panel). Green (gray): d at -15% (+15%) of the aforementioned value.

#### 7 Transport characterization of the graphene-on-diamond device

In Fig. S7, we show resistance R as a function of the gate voltage  $V_g$  and carrier density n for the graphene-on-diamond device, obtained with two-terminal measurement. The location of the charge neutrality point (Dirac point)  $V_D$  is determined from location of the peak resistance. Carrier density n is determined using  $n = C_g(V_g - V_D)$ , where  $C_g = \varepsilon_0 \varepsilon_r/(et)$  is the gate capacitance per area, with  $\varepsilon_0$  the permittivity of free space,  $\varepsilon_r$  the dielectric constant, and t the thickness of the dielectric. For the graphene-on-diamond device,  $\varepsilon_r = 4$  and t = 13nm are used for the hBN gate dielectric.

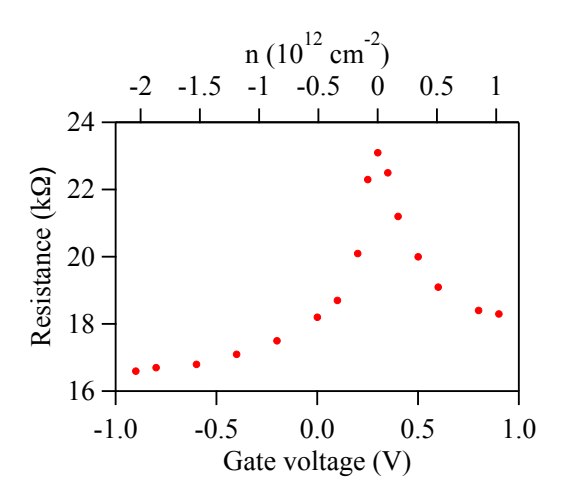


Figure S7: Resistance R as a function of the gate voltage  $V_g$  and carrier density n obtained from two-terminal measurement.

#### 8 Transport characterization of devices for scanning measurement

In Fig. S8, we show resistivity  $\rho$  as a function of carrier density n for three of the four devices shown in Fig. 2f of the main text. Resistivity was obtained with four-terminal measurements. The location of the charge neutrality point (Dirac point)  $V_D$  is determined from location of the peak resistance. Carrier density n is determined using  $n = C_g(V_g - V_D)$ , where  $C_g = \varepsilon_0 \varepsilon_r/(et)$  is the gate capacitance per area, with  $\varepsilon_0$  the permittivity of free space,  $\varepsilon_r$  the dielectric constant, and t the thickness of the dielectric. For the devices made on the standard SiO<sub>2</sub>/Si substrates,  $\varepsilon_r = 3.9$  and t = 285 nm are used.

For the device corresponding to the second (from the left) data in Fig. 2f of the main text, the geometry of the device precluded a four-terminal measurement of the resistivity. However, because photo-doping brings the system to the Dirac point in steady state, the magnetometry measurements performed on this device were at the Dirac point. The last two sets of data (from the right) of Fig. 2f of the main text correspond to the same physical device: initial transport characteristics are shown in the middle panel of Fig. S8, and later, altered characteristics are shown in the right panel of Fig. S8. The later state of the device has a significantly broader  $\rho$  vs n and much lower peak resistivity, indicating higher carrier density inhomogeneity. Therefore, we consider the two states as two distinct devices.

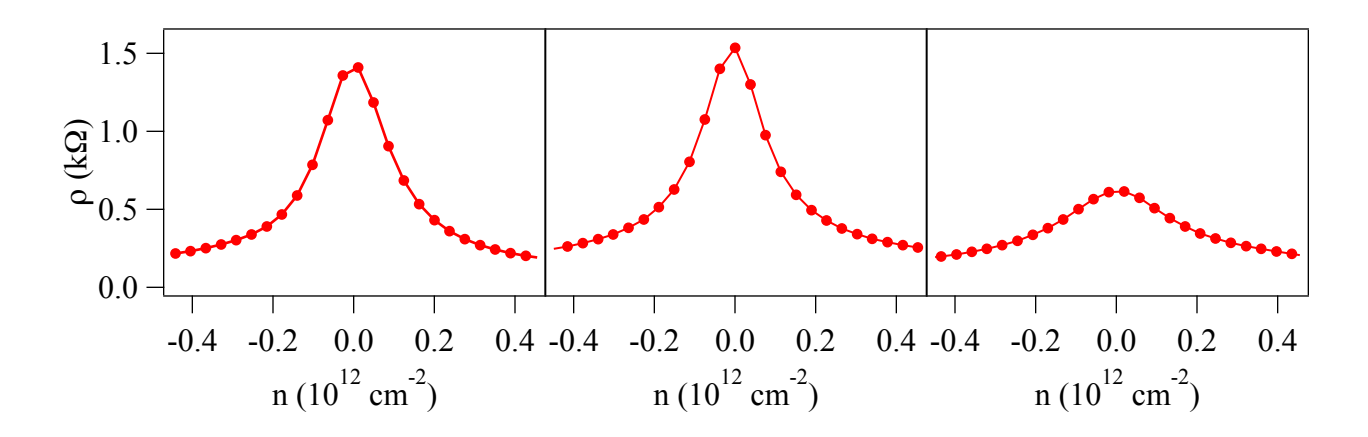


Figure S8: Resistivity  $\rho$  as a function of carrier density n for three of four graphene devices shown in Fig. 2f of the main text. From the left to right, each panel corresponds to the (starting from left) first, third, and fourth data set shown in Fig. 2f of the main text. Resistivity was obtained using four-terminal measurements.

#### 9 Variation of viscous profile at different Gurzhi Lengths

The linearized electronic Navier Stokes equation<sup>4</sup> for the current density  $\bf{J}$  is

$$-\nu\nabla^2 \mathbf{J} + \frac{1}{\tau_{\rm mr}} \mathbf{J} = e^2 \frac{n}{m} \mathbf{E} \,, \tag{S11}$$

where  $\nu$  is the kinematic viscosity, e is the electronic charge,  $\tau_{\rm mr}$  is the momentum-relaxing time, m is the effective mass, and  ${\bf E}$  is the bias electric field. For electronic carriers in graphene,  $m=\hbar\sqrt{\pi n}/v_{\rm F}$ , where  $v_{\rm F}=10^6\,{\rm m/s}$  is the Fermi velocity. A flow along the y-direction  ${\bf J}=(0,J_y(x))$  and under no-slip boundary condition,  $J_y(x=\pm W/2)=0$  has following current density

$$J_y(x) = \frac{e^2 v_F \tau_{\rm mr}}{\hbar} \sqrt{\frac{n}{\pi}} E \left( 1 - \frac{\cosh(x/D_\nu)}{\cosh(W/(2D_\nu))} \right) , \qquad (S12)$$

where  $D_{\nu} \equiv \sqrt{\nu \tau_{\rm mr}}$ . One can then obtain the conductivity defined as  $\sigma \equiv I/(WE)$  where  $I = \int dx J_y(x)$ :

$$\sigma = \frac{e^2 v_{\rm F} \tau_{\rm mr}}{\hbar} \sqrt{\frac{n}{\pi}} \left( 1 - \frac{2D_{\nu}}{W} \tanh\left(\frac{W}{2D_{\nu}}\right) \right) . \tag{S13}$$

In Fig. S9, we show profiles from the solution of the electronic Navier Stokes equation with different values of  $D_{\nu}/W$ . For  $D_{\nu}/W \ll 1$ , the current density approaches a uniform profile  $J_y = \sigma_0 E$  and the conductivity  $\sigma = \sigma_0 \equiv e^2 \tau_{\rm mr} n/m$  becomes the Drude conductivity. For  $D_{\nu}/W \gg 1$ , the current density approaches the ideal Poiseuille profile  $J_y(x) = \frac{e^2 v_{\rm F}}{2\hbar \nu} \sqrt{\frac{n}{\pi}} E\left(\left(\frac{W}{2}\right)^2 - x^2\right)$ , and the conductivity  $\sigma = e^2 n W^2/(12m\nu)$  has the  $\sim W^2/\nu$  scaling. For  $D_{\nu}/W = 0.3$ , the current density approaches within 5% of the ideal Poiseuille profile, while for  $D_{\nu}/W > 0.5$ , the current density approaches within 2% of the ideal Poiseuille profile.

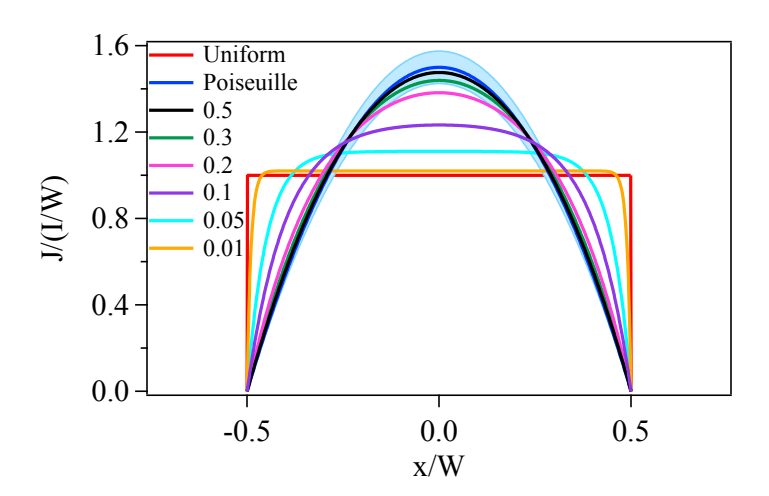


Figure S9: Solution of the electronic Navier Stokes equation with different values of  $D_{\nu}/W$ . The band around the ideal Poiseuille profile is 5%. The current density is normalized by the average flux I/W, and the spatial position is normalized by W.

## 10 Comparison of measured current profile to the flow of non-interacting electrons with diffuse boundary

For a system of non-interacting ( $\tau_{\rm pp}=\infty$ ) electrons moving in a channel -W/2 < x < W/2 with completely diffusive boundary, the flow profile develops a curvature in the regime when the momentum-relaxing mean free path is on the order of the width,  $l_{\rm mr}\approx W$ . In the main text, we compared the NV measured profile in graphene at the charge neutrality point (CNP) to the non-interacting case, and concluded that the non-interacting case cannot explain our measurement. In this section, we discuss the details of the calculation of non-interacting profiles.

The derivation of the current profile of non-interacting electrons in a channel with diffuse boundary can be done following previous work (see, e.g., ref. <sup>5</sup> and references therein). The local current density is given by

$$\mathbf{J}(x) = eg \int \frac{d^2p}{(2\pi)^2} \mathbf{v} f(x, \mathbf{p}), \qquad \mathbf{v} = \partial_{\mathbf{p}} \varepsilon, \tag{S14}$$

where e=-|e| is the electron charge, g=4 is the spin-valley degeneracy,  $\varepsilon=\varepsilon(\mathbf{p})$  is the quasiparticle energy as a function of momentum  $\mathbf{p}$ , and  $f(x,\mathbf{p})$  is the steady-state quasiparticle distribution function. It is convenient to write the deviation of f from the equilibrium Fermi-Dirac distribution  $f_0(\varepsilon)=\left[e^{(\varepsilon-\varepsilon_F)/T}+1\right]^{-1}$  in the form

$$f(x, \mathbf{p}) - f_0(\varepsilon) = \left(-\frac{df_0}{d\varepsilon}\right) F.$$
 (S15)

If the temperature T is much smaller than the Fermi energy  $\varepsilon_F = \varepsilon(p_F)$ , the dependence of F on  $|\mathbf{p}|$  proves to be weak, so that  $F = F(x, \theta)$  where  $\theta$  is the angle between vector  $\mathbf{p}$  and the y-axis.

Accordingly, the current density is given by

$$\mathbf{J}(x) = e \frac{dn}{d\varepsilon_F} \int_{-\pi}^{\pi} \frac{d\theta}{2\pi} \mathbf{v} F(x, \theta), \qquad \mathbf{v} = (-v_F \sin \theta, v_F \cos \theta),$$
 (S16)

where  $n=g\int f_0(\varepsilon)\,d^2p/(2\pi)^2$  is the electron density and  $v_F=d\varepsilon_F/dp_F$  is the Fermi velocity. Adopting the relaxation-time approximation for bulk scattering, we obtain the linearized Boltzmann kinetic equation for F:

$$v_x \partial_x F - e v_y E = -\frac{F - \overline{F}}{\tau_{\text{mr}}}, \qquad \overline{F} \equiv \int_{-\pi}^{\pi} \frac{d\theta}{2\pi} F.$$
 (S17)

It is easy to see that F must be odd under reflection with respect to the x-axis:  $|\theta| \to \pi - |\theta|$ . This implies that  $\overline{F} = 0$ , so that the electron density and the electric field E are uniform in the channel. Equation (S17) becomes

$$\sin\theta \,\partial_x F + \frac{F}{l_{\rm mr}} = eE\cos\theta. \tag{S18}$$

We need to solve this equation subject to the suitable boundary conditions (BC) at the edges. For the case of purely diffuse scattering, the quasiparticle flux reflected from the edges is isotropic. Thus, the BC at x = W/2 edge is  $F(W/2, \theta) = \text{const}$  at  $0 < \theta < \pi$ . Flux conservation fixes this constant to be

$$F(W/2, \theta) = \frac{1}{2} \int_{-\pi}^{0} F(W/2, \theta') \sin \theta' d\theta', \qquad 0 < \theta < \pi.$$
 (S19)

A similar boundary condition, for angles  $-\pi < \theta < 0$ , holds at x = -W/2 edge. The desired solution is therefore

$$F(x,\theta) = eEl_{\rm mr}\cos\theta \left\{ 1 - \exp\left[ -\frac{W/(2l_{\rm mr})}{|\sin\theta|} + \frac{x/l_{\rm mr}}{\sin\theta} \right] \right\}.$$
 (S20)

Substituting this expression into Eq. (S16), we obtain, after some elementary transformations,

$$\frac{J_y(x)}{e\sigma_0 E} = 1 - G\left(\frac{W + 2|x|}{2l_{\rm mr}}\right) - G\left(\frac{W - 2|x|}{2l_{\rm mr}}\right), \qquad G(z) \equiv \frac{2}{\pi} \int_{1}^{\infty} \frac{du}{u^3} \sqrt{u^2 - 1} e^{-zu}, \quad (S21)$$

where  $\sigma_0 = e^2 n l_{\rm mr}/(v_{\rm F} m)$  is the standard Drude conductivity.

Function G(z) monotonically decreases at z > 0 and has the following asymptotic behavior:

$$G(z) \simeq \frac{1}{2} - \frac{2}{\pi} z \ln\left(\frac{2e^{-\gamma}}{z}\right) - \frac{z^2}{2} + \frac{1}{6\pi} z^3 \left[\ln\left(\frac{2e^{-\gamma}}{z}\right) + \frac{7}{3}\right], \qquad z \ll 1,$$
 (S22)

$$\simeq \sqrt{\frac{2}{\pi z^3}} e^{-z}, \qquad z \gg 1, \qquad (S23)$$

where  $\gamma=0.577$  is the Euler constant. The upper line is relevant if the scattering is dominated by the edges (i.e. ballistic limit),  $l_{\rm mr}\gg W$ . The lower line is useful if the transport is limited by the bulk scattering (i.e. Ohmic limit),  $l_{\rm mr}\ll W$ . In both such limits the current density enhancement  $J_y(0)W/I$  at the center of the channel becomes small.

In general, this profile has some curvature, which is maximal in the regime of  $l_{\rm mr}\approx W$ . In Fig. S10, we show the profiles at various values of  $l_{\rm mr}/W$  and compare to an ideal Poiseuille flow. We see that the non-interacting profiles begin as a uniform profile for  $l_{\rm mr}/W\ll 1$ , develop a curvature that is maximal at  $l_{\rm mr}/W\approx 1$ , and then flattens again as  $l_{\rm mr}/W\gg 1$ . In Fig. S11, we show the peak (central) value of  $J_y/(I/W)$  as a function of  $l_{\rm mr}/W$  in order to quantify the curvature of the profile. The maximum occurs at  $l_{\rm mr}/W=0.625$ , though there is little change in the range of  $l_{\rm mr}/W\sim 0.5$ -1. From both Figs. S10 and S11, we see that even with the maximal curvature at  $l_{\rm mr}/W=0.625$ , the non-interacting profile still significantly deviates from the ideal viscous case. In Fig. 2e of the main text, we compared an experimental profile at the CNP to both the ideal viscous profile and the non-interacting profile in graphene, which instead matches well to the viscous profile.

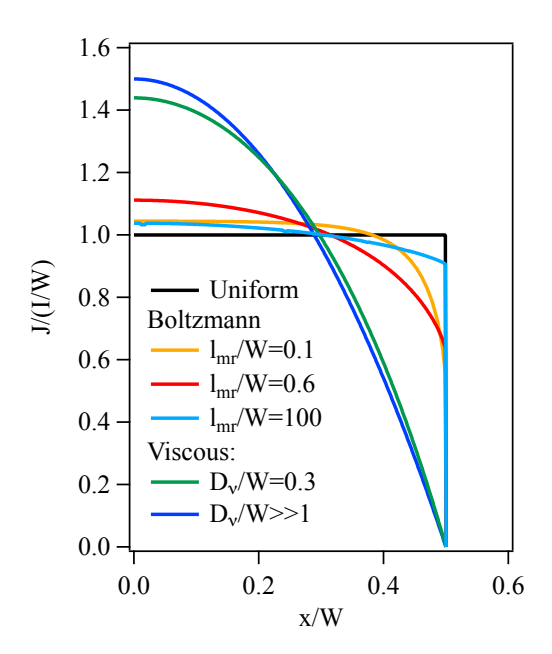


Figure S10: Comparison of hydrodynamic profiles with  $D_{\nu}/W=0.3,\,\infty$  and non-interacting profiles with  $l_{\rm mr}/W$ =0.1, 0.6, and 100.

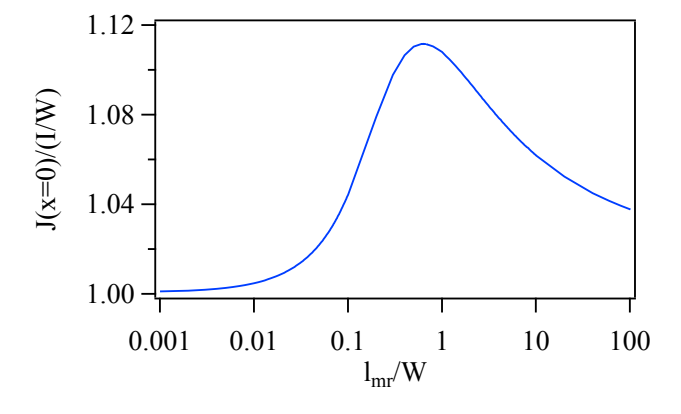


Figure S11: Peak (central) value of J/(I/W) of non-interacting profiles as a function of  $l_{\rm mr}/W$ .

#### 11 Validity of hydrodynamics in graphene at room temperature

At elevated temperatures, the dominant mechanism for momentum-relaxation is electron-phonon scattering. For hBN-encapsulated graphene, the associated momentum-relaxing mean free path  $l_{\rm mr}\approx 1\,\mu{\rm m}$  (refs.  $^{6\text{-}8}$ ) corresponds to  $\tau_{\rm mr}=l_{\rm mr}/v_{\rm F}\approx 1\,{\rm ps}$ . From the main text, we have  $\tau_{\nu}=0.19-0.39\,{\rm ps}$ ;  $\tau_{\rm pp}$  should be on the same order and hence is small compared to  $\tau_{\rm mr}$ . We also note that the particle-particle collision mean free path is  $l_{\rm pp}\equiv\tau_{\rm pp}v_{\rm F}\sim190-390\,{\rm nm}$ , corresponding to a Knudsen number  ${\rm Kn}\equiv l_{\rm pp}/W\sim0.19-0.39$ , which is small compared to unity. Together, these two conditions justify the hydrodynamic limit. As observed in this work and in ref.  $^8$ , for the usual range of carrier density  $n<10^{12}\,{\rm cm}^{-2}$  accessed in a graphene experiment,  $\nu\sim0.1-0.4\,{\rm m}^2/{\rm s}$ , which corresponds to  $D_{\nu}\approx300-600\,{\rm nm}$ . For  $W=1\,\mu{\rm m}$ , the resulting  $J_y$  calculated with Eq. 1 of the main text is within 4% to 1% of an ideal viscous profile with the same total current. This is consistent with our observation that there is no discernible variation in the current profile at different carrier densities.

#### 12 Effect of photo-doping on scanning magnetometry experiment

Exposure to light is known to lead to photo-induced doping in an hBN-encapsulated graphene device fabricated on an  $SiO_2$ /doped Si substrate<sup>9,10</sup>. The mechanism is that defects residing in hBN are photo-dissociated, leading to free positive and negative charges that can migrate within the hBN layer. At any value of gate voltage  $V_g$ , the free charges experience the electric field and migrate accordingly. The charges that migrate towards the graphene dope the graphene; however, the charges that migrate towards  $SiO_2$  cannot exit the hBN layer, remain trapped in hBN, and serve to screen the electric field<sup>11,12</sup>. Hence, upon light exposure, the system moves towards the CNP over time, and the steady state is the CNP. Nevertheless, the rate is slow enough that we can obtain scanning NV magnetic measurements as a function of carrier density range. In this section, we describe the relevant analysis to examine the effect of photo-doping in scanning measurement.

In scanning NV magnetometry, photo-induced doping occurs as the graphene device is exposed to the NV-excitation light scattered from the diamond probe. We observe photo-doping dynamics with the following experiment. With the probe retracted (about  $10\,\mu\mathrm{m}$  above the device) and light focused on the probe, we set  $V_g$  to a finite value, and monitor the resistivity  $\rho$  as a function of time. The density-dependent transport curve  $\rho$  vs n of this device is shown in the middle panel of Fig. S8. In Fig. S12, we show  $\rho$  as a function of time for  $V_g = -10\,\mathrm{V}$  (left panel) and  $V_g = +10\,\mathrm{V}$  (right panel). In both cases, the resistivity increases and saturates at the resistivity associated with the CNP  $\approx 1.5\,\mathrm{k}\Omega$  (see the middle panel of Fig. S8). This indicates the evolution of the system towards CNP and that the CNP is the steady state under light illumination.

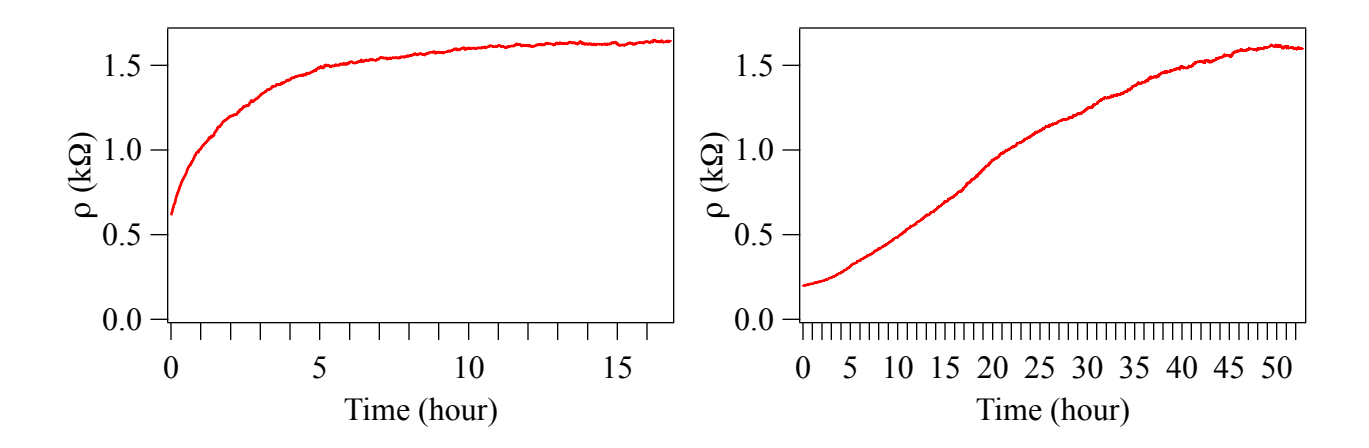


Figure S12: Time-dependent evolution of resistivity  $\rho$  under exposure to NV-excitation light scattered from the diamond probe. The measurement is done with the probe retracted at about  $10\,\mu\mathrm{m}$  above the device. Time evolution is measured with  $V_g$  set to  $-10\,\mathrm{V}$  (left) and  $+10\,\mathrm{V}$  (right). Note that while ref.  $^9$  observed photo-induced doping to occur only for  $V_g < 0$  at 77 K, here we observe photo-induced doping regardless of the sign of  $V_g$  at room temperature. Our observation is consistent with the result of ref.  $^{10}$ .

Once the system has been photo-doped to the CNP, it is stable under light illumination. In the left panel of Fig. S13, we show  $\rho$  measured throughout the course of a scanning magnetometry measurement when the device has been photo-doped to the CNP. Negligible variation in  $\rho$  is observed.

Photo-induced doping presents complication for a scanning magnetometry measurement away from the CNP. The time scale of the dynamics presented in Fig. S12 is on the order of hours, but this is under the situation when the probe is retracted. When the probe is on the device,

the evolution becomes significantly faster. Nevertheless, the dynamics is slow enough that during a scanning magnetometry measurement, which lasts about 1.5 hours, the system evolves across a range of carrier density, but does not completely reach the CNP. For the data presented in Fig. 4a of the main text, we first photo-dope the system to shift the CNP to  $V_g = -20\,\mathrm{V}$ . Then, we set  $V_g = 0\,\mathrm{V}$ , and perform scanning magnetometry measurements. Before and after each set of scanning magnetometry measurements, we monitor the resistivity  $\rho$  to determine the carrier density range that the system has evolved across by matching the measured resistivity to the transport curve shown in the middle panel of Fig. S8. In the right panel of Fig. S13, we show the same transport curve as in the middle panel of Fig. S8, and shade the ranges of carrier density that the system has evolved across during the two measurements at finite carrier density shown in Fig. 4a of the main text. The carrier density range is  $n = 0.3 - 1.5 \times 10^{12}\,\mathrm{cm}^{-2}$  and  $n = 0.1 - 0.3 \times 10^{12}\,\mathrm{cm}^{-2}$  respectively.

Unlike a device where gating is provided by a Si back gate separated from the device with an SiO<sub>2</sub> layer, a device where gating is provided by a graphite gate, separated from the graphene only by an hBN layer, does not undergo photo-induced doping<sup>13</sup>. Therefore, the graphene-on-diamond device, where gating is provided by a graphite top gate separated from the graphene by an hBN layer, does not suffer from photo-induced doping.

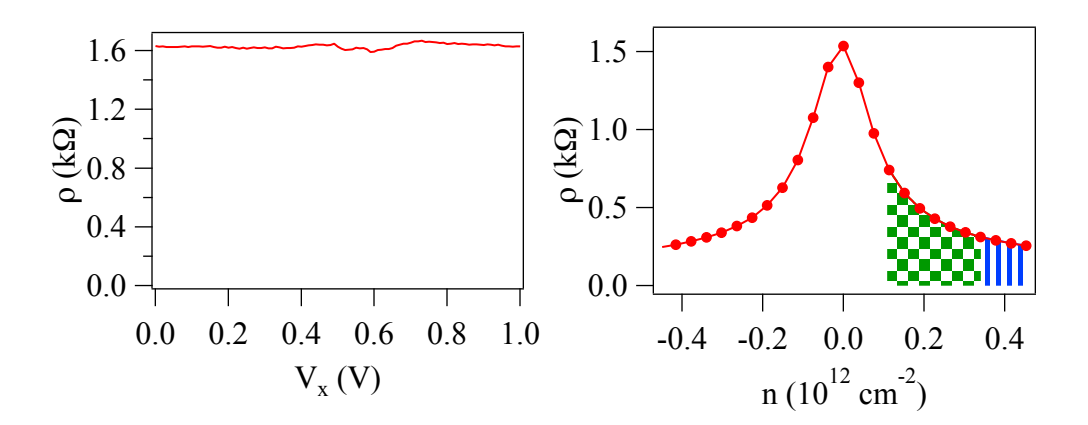


Figure S13: Left panel: resistivity monitored as a function of piezo scanner voltage during a scanning NV magnetometry measurement. Right panel: transport curve  $\rho$  vs n from the middle panel of Fig. S8, and carrier density range (green checkers and blue vertical stripes) covered by the two scanning magnetometry measurements at finite carrier density shown in Fig. 4a of the main text. The carrier density ranges are  $n=0.3-1.5\times 10^{12}\,\mathrm{cm^{-2}}$  and  $n=0.1-0.3\times 10^{12}\,\mathrm{cm^{-2}}$ .

#### 13 Comparison of current reconstruction methods for scanning magnetometry

In this section, we compare the current reconstruction method for scanning magnetometry described in the main text with an alternative approach where one directly inverts the Biot-Savart law in Fourier space (Eqs. S3, S4, S6). We refer to the latter approach as Fourier inversion. We show that the main text method gives the same bulk current profile as Fourier inversion; however, unlike Fourier inversion, the main text method preserves sharp edges in the current profile (if present) without amplifying noise.

In Fig. S14, we show the current profile in graphene from Fig. 2e of the main text along with current profiles obtained from the same scanning magnetometry data using the Fourier inversion method for several values of standoff distance d. Regularization is achieved via placing a cutoff  $k_c$  in Fourier space, with  $k_c$  chosen in each case such that the variation in the background (i.e., for |x| > W/2) is similar to the peak error bar from the data of Fig. 2e. Over the range of d expected for the experiment, we see that the current profile obtained with the main text method is consistent with that obtained from Fourier inversion.

In Fig. S15, we show the dependence on Fourier cutoff  $k_c$  for  $d=30\,\mathrm{nm}$ . The qualitative shape of the current density - a parabolic profile - is insensitive to the choice of  $k_c$ , which is consistent with the expectation for a smooth profile. The only difference  $k_c$  makes is the amount of noise and the prominence of the dip feature close to the center of the profile. The optimal cutoff for this measurement is  $k_c/(2\pi)=3\,\mu\mathrm{m}^{-1}$ .

In Fig. S16, we show the current profile in Pd from Fig. 2e of the main text along with current profiles obtained from the same data using the Fourier inversion method with  $d = 70 \,\mathrm{nm}$  and for several values of  $k_c$ . For low  $k_c$ , the influence of high spatial frequency noise on the reconstruction is minimal, but sharp features in the current profile are washed out. As one increases  $k_c$ , one begins to recover sharp edges, but when the sharp features are comparable to those of the reconstructed current profile from the main text (lower right panel), high spatial frequency noise is severely amplified. Lastly, we see that the width of the rise at the edges is given by  $1/k_c$ .

From this analysis, we see that the main text reconstruction method gives the same result as Fourier inversion when there are no sharp spatial features in the current profile. Compared to Fourier inversion, the main text method is able to preserve sharp features without amplifying noise.

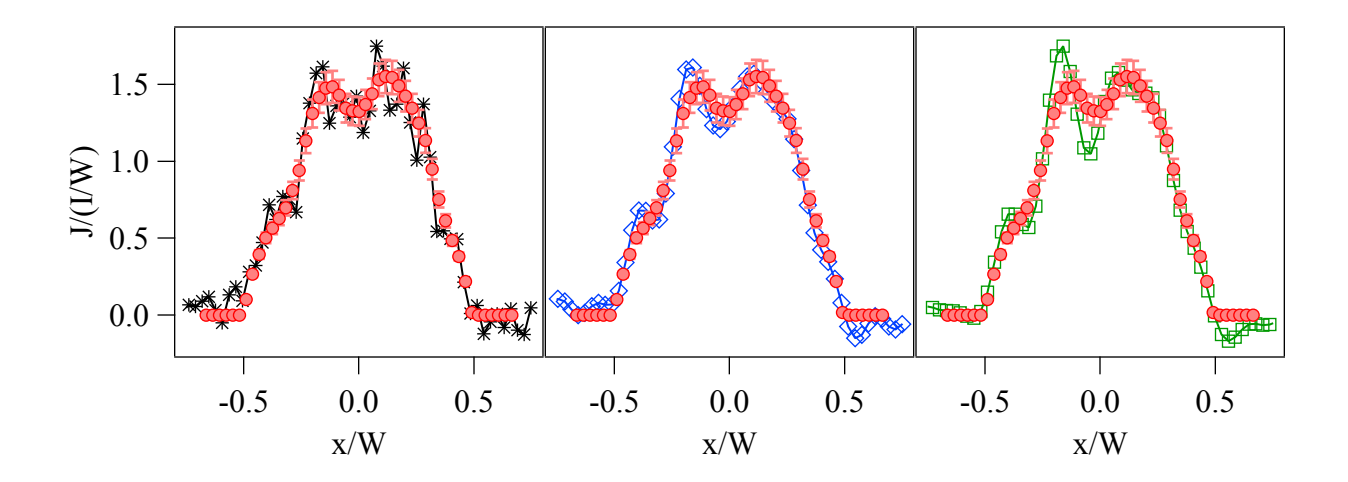


Figure S14: Comparison of current profile in graphene from Fig. 2e of the main text (red circles) to current profile extracted with Fourier inversion using several standoff distances d. Left panel: black stars are for  $d=15\,\mathrm{nm}$ . Middle panel: blue open diamonds are for  $d=30\,\mathrm{nm}$ . Right panel: green open squares are for  $d=50\,\mathrm{nm}$ . In each case where Fourier inversion is applied, a cutoff in Fourier space is chosen such that the resulting noise in the background is comparable to the peak error bar of the red data points.

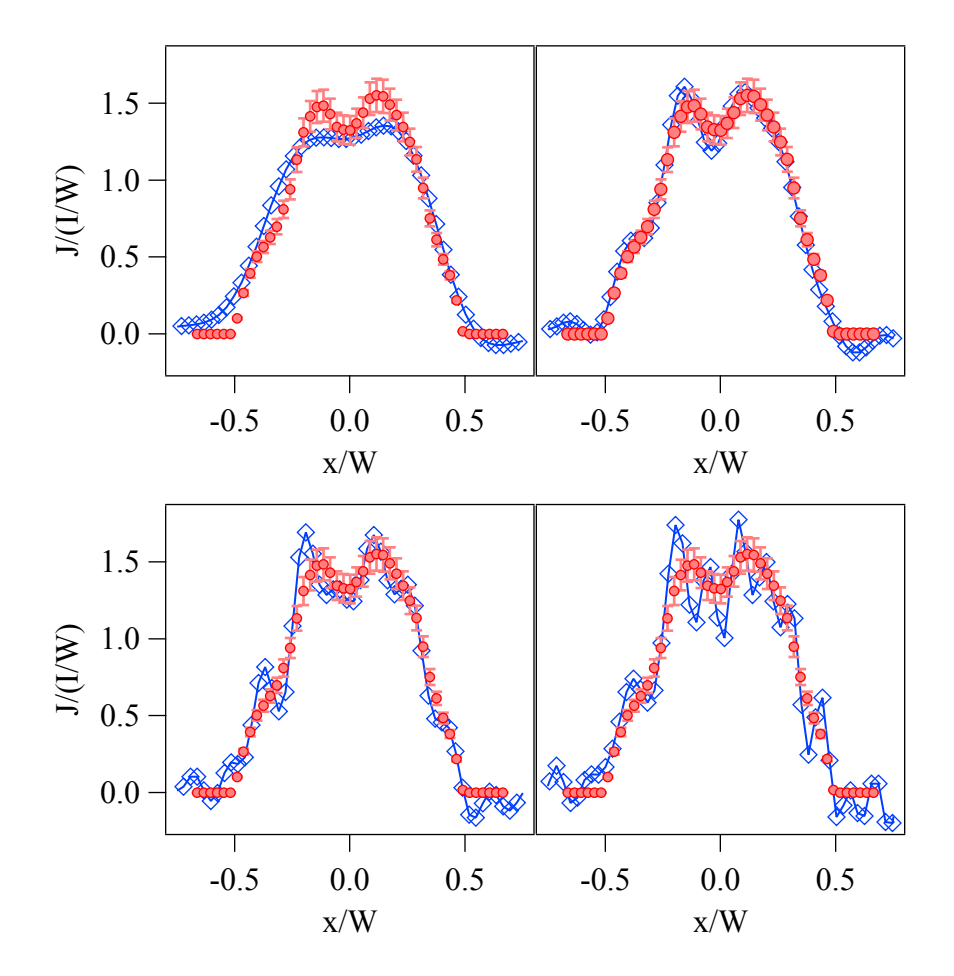


Figure S15: Comparison of current profile in graphene from Fig. 2e of the main text (red circles) to current profile extracted with Fourier inversion (blue diamond) at  $d=30\,\mathrm{nm}$  using several Fourier cutoffs  $k_c$ . Upper left:  $k_c/(2\pi)=1.7\,\mu\mathrm{m}^{-1}$ . Upper right:  $k_c/(2\pi)=3\,\mu\mathrm{m}^{-1}$ . Lower left:  $k_c/(2\pi)=4.4\,\mu\mathrm{m}^{-1}$ . Lower right:  $k_c/(2\pi)=5.7\,\mu\mathrm{m}^{-1}$ .

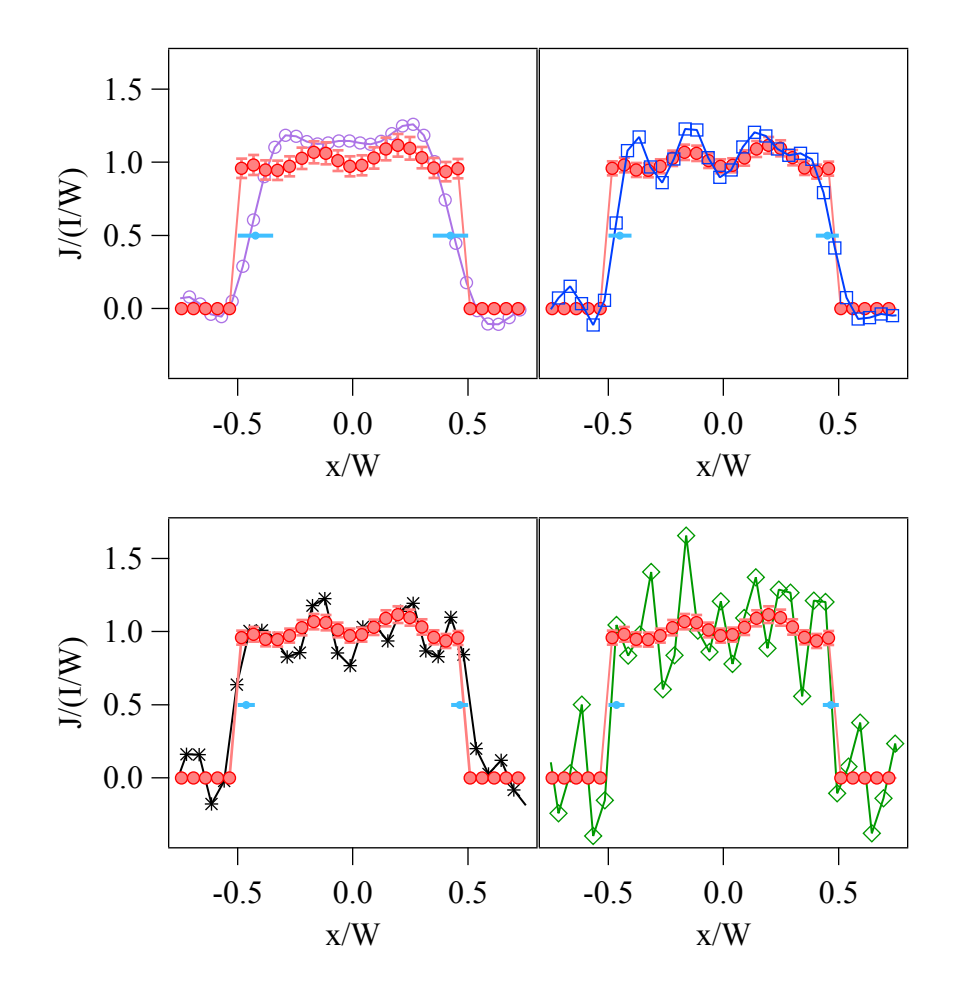


Figure S16: Comparison of current profile in Pd from Fig. 2e of the main text (red circles) to current profile extracted with Fourier inversion at  $d=70\,\mathrm{nm}$  using several Fourier cutoffs  $k_c$ . Upper left (purple):  $k_c/(2\pi)=2.1\,\mu\mathrm{m}^{-1}$ . Upper right (blue):  $k_c/(2\pi)=3.2\,\mu\mathrm{m}^{-1}$ . Lower left (black):  $k_c/(2\pi)=4.3\,\mu\mathrm{m}^{-1}$ . Lower right (green):  $k_c/(2\pi)=4.6\,\mu\mathrm{m}^{-1}$ . For each panel, the light blue points are located at  $\pm(W-k_c^{-1})$ , and the light blue bars extend from the light blue points with a length  $1/k_c$ .

#### 14 Heating due to laser and microwave delivery in wide-field imaging

To estimate heating due to laser and microwave delivery, we use the Fourier law  $\mathbf{q}=-k\nabla T$ , where q is the heat flux and k is the thermal conductivity. Here, we use  $k=2200\,\mathrm{W/(mK)}$  for diamond. If the heat is being deposited at a power Q over an area  $\Delta x^2$ , where  $\Delta x$  is the characteristic length scale of the heating, then based on the Fourier law we can write  $Q/\Delta x^2\approx k\Delta T/\Delta x$  and hence  $\Delta T\approx Q/(k\Delta x)$ .

For wide-field imaging, about  $10\,\mathrm{mW}$  of laser illuminates an area of about  $5\,\mu\mathrm{m}$  in diameter. If we assume the laser is completely absorbed on the diamond surface, then with  $Q\approx 10\,\mathrm{mW}$  and  $\Delta x\approx 5\,\mu\mathrm{m}$ , we get an upper bound on the temperature change to be  $\Delta T\lesssim 1\,\mathrm{K}$ .

Microwave delivery for wide-field imaging consists of a -35 dBm signal amplified at 45 dB gain. Therefore, about  $10\,\mathrm{mW}$  of power is sent through the microwave delivery. Once again, if we assume this power is entirely deposited on the diamond in the vicinity of the device, and using the dimension of the microwave delivery to estimate  $\Delta x \approx 10\,\mu\mathrm{m}$ , we get  $\Delta T \lesssim 1\,\mathrm{K}$ .

In both cases, we see that heating due to laser and microwave delivery is negligible in widefield imaging.

# 15 Estimate fluctuation potential for high impurity device

One of the devices measured has higher charge impurity, as shown by the lower resistivity at the Dirac peak. The current profile for this device is shown as the right-most profile in Fig. 2f and its transport curve  $\rho$  vs. n is shown in the right-most panel of Fig. S8. In this section, we estimate the fluctuation potential  $\delta\mu$  as a measure of the impurity level for this device.

It is insightful to plot the transport measurement data in the form of conductivity  $\sigma$  vs. Fermi wave vector  $k_{\rm F}=\sqrt{\pi n}=E_{\rm F}/(\hbar v_{\rm F})$  (Fig. S17). For both the standard device and high impurity device, the data shows that initially for small  $k_{\rm F}$ ,  $\sigma$  remains close to constant, and for large  $k_{\rm F}$ , there is a linear trend that extrapolates to an x-intercept corresponding to  $k_{\rm F}=k_{\rm B}T/(\hbar v_{\rm F})$ . The difference between the standard device and the high impurity device is that the latter has a higher minimal conductivity.

In the viscous Poiseuille  $(D_{\nu}\gg W)$  regime, the conductivity can be written as  $\sigma=\mathcal{A}E_{\rm F}/\nu$  where  $\mathcal{A}=e^2W^2/(12\pi\hbar^2)$ . Note that the same form  $\sigma\propto E_{\rm F}$  can be written in the Ohmic case, except that the relevant quantity that determines transport is  $\tau_{\rm mr}$  instead of  $\nu$ , and that W disappears from the dependence. The data of  $\sigma$  vs  $k_{\rm F}$  data can be described by the following model:

$$\sigma = \begin{cases} \mathcal{A}(k_{\rm B}T + \delta\mu)/\nu_{\rm DF} & E_{\rm F} < k_{\rm B}T + \delta\mu \\ \mathcal{A}(E_{\rm F} - k_{\rm B}T)/\nu_{\rm FL} & E_{\rm F} > k_{\rm B}T + \delta\mu \end{cases}$$
(S24)

In this model,  $\nu$  is treated as taking on a constant value  $\nu_{\rm DF}$  near the CNP (the Dirac fluid regime), and another constant value  $\nu_{\rm FL}$  in the finite-density Fermi-liquid regime. Such

approximation is justified from the result shown in Fig. 4b.

In this model, the minimal conductivity  $\sigma_{\min} \sim (k_{\rm B}T + \delta\mu)/\nu_{\rm DF}$ . Assuming  $\nu_{\rm DF}$  is an intrinsic property of the system and hence is independent of inhomogeneity, what sets  $\sigma_{\min}$  at a given temperature is  $\delta\mu$ . Therefore, when comparing two minimal conductivities, we have  $\sigma_{\min,1}/\sigma_{\min,2} = (k_{\rm B}T + \delta\mu_1)/(k_{\rm B}T + \delta\mu_2)$ . We use two values of  $\delta\mu$  for the standard device:  $\delta\mu = 0$  and  $\delta\mu = 50$  K, which is typical for encapsulated device<sup>14</sup>. This allows us to estimate the fluctuation potential for the high impurity device:  $\delta\mu = 450 - 570$  K, which is large compared to the thermal energy.

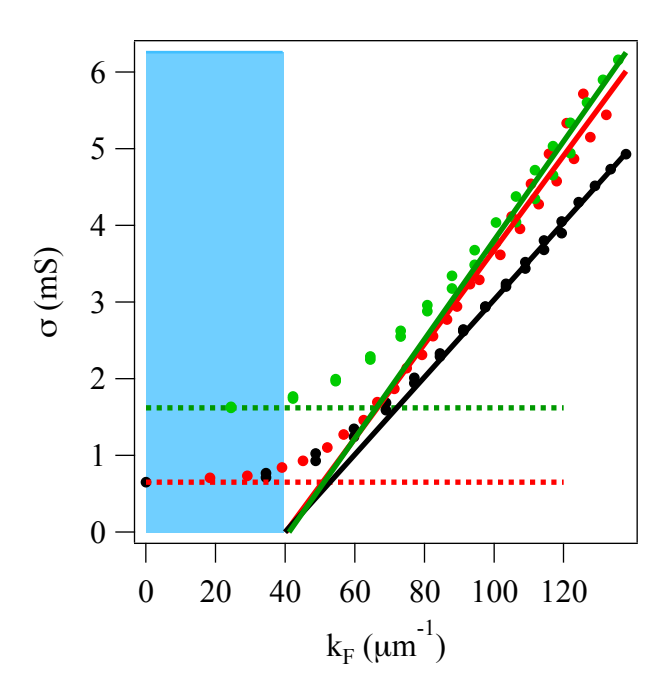


Figure S17: Conductivity  $\sigma$  as a function of Fermi wave vector  $k_F = \sqrt{\pi n}$ . Red, black, and green circles correspond to transport measurements shown in the left, middle, and right panels of Fig. S8. Red and black data are from standard devices, and green data is from the high-impurity device. The corresponding solid curves are linear fits to the data for  $k_F > 100 \, \mu \text{m}^{-1}$ . Shaded blue region corresponds to  $k_F < k_{\rm B}T/(\hbar v_{\rm F})$ . Red (green) horizontal dashed lines correspond to the minimal conductivity for the standard devices (high-impurity device).

# 16 Transport regime of Pd

Here we substantiate that the transport regime of the Pd wire is Ohmic. Refs.  $^{15,16}$  have each obtained palladium  $l_{\rm mr}$  to be 9 nm and 25 nm respectively. The Fermi energy is  $E_{\rm F}=8.16\,{\rm eV}$ , and with effective mass  $m^*/m=0.4$ , this gives us the Fermi velocity  $v_{\rm F}=2.7\times10^6\,{\rm m/s}$ . We then have the elastic (momentum-relaxing) scattering time  $\tau_{\rm mr}=3-9\,{\rm fs}$ . The mobility  $\sim 10{\rm cm}^2/({\rm Vs})$  is four magnitude lower compared to that of high quality graphene device such as in our experiment. For the Fermi liquid regime valid for Pd, the electron-electron scattering time can be estimated  $\tau_{\rm ee}\sim\hbar E_{\rm F}/(k_{\rm B}T)^2=8\,{\rm ps}\gg\tau_{\rm mr}$ . With such a short momentum-relaxing scattering time compared to the electron-electron scattering time, transport in Pd is diffusive (Ohmic).

# 17 Estimate of the slip-length

Poiseuille current flow only occurs with a no-slip boundary condition  $u_y(x=\pm W/2)=0$ , where W is the channel width. In general, the boundary condition can be parameterized by the slip-length  $\zeta$ , defined as  $\zeta\equiv\left|\frac{du_y}{dx}\right|/u_y$  evaluated at the boundary  $^{17}$ . A no-slip boundary condition applies for  $\zeta\ll W$ , where the other limit is the no-stress boundary condition  $\zeta\gg W$ . In the case of no-stress boundary condition, current flow in a channel is uniform despite the presence of viscosity.

The boundary condition for (lithographically patterned) graphene was not known prior to our work. Viscous flow of an electron fluid in doped graphene has been explored either via a vortex whirlpool detected using a negative vicinity voltage<sup>8,18,19</sup> or superballistic conduction measured with a point contact<sup>20</sup>. Formation of a vortex whirlpool is insensitive to the boundary condition<sup>8</sup>. Superballistic flow through a point contact has a profile that is analogous to Poiseuille flow across a channel, but does not require a no-slip boundary condition; e.g., the analysis of ref. <sup>20</sup> was performed with a no-stress boundary condition.

In our graphene experiments, we find that the current continuously decreases away from the center of the channel, vanishing at the boundary. This observation indicates a no-slip boundary condition at the room temperature. Kiselev and Schmalian<sup>17</sup> estimate  $\zeta \approx 0.6 l_{\rm pp}$  for the diffuse limit likely appropriate for lithographically patterned graphene. The authors also discuss a nearly specular limit with  $\zeta \approx 0.008 \left(\frac{\lambda_T^3}{h^2h'}\right) l_{\rm pp}$ . Here,  $\lambda_T = v_{\rm F}\hbar/(k_{\rm B}T)$  is the thermal wavelength and the two length scales h and h' are the roughness of the edge. The authors use  $h = h' = 250 \,\text{Å}$ .

Thus in the nearly specular limit, the ratio  $\lambda_T^3/(h^2h')\approx 1$  and  $\zeta\approx 0.008l_{\rm pp}$ . This is much smaller compared to the diffuse limit, and since we are interested to establish an upper bound on  $\zeta$  from the authors' estimate, it is appropriate to consider the diffuse limit.

In order to estimate  $\zeta$ , we need  $l_{\rm pp}=v_{\rm F}\tau_{\rm pp}$ . The viscous scattering time  $\tau_{\nu}$  determined in our work is not the same as  $\tau_{\rm pp}$ . However,  $\tau_{\rm pp}$  is measured in ref. <sup>21</sup> to be  $\tau_{\rm pp}=5\tau_{\hbar}$  so we use that value here. At  $T=300\,{\rm K}$  we have  $\tau_{\rm pp}=127\,{\rm fs}$  and hence  $l_{\rm pp}=127\,{\rm nm}$ . This gives  $\zeta\approx76\,{\rm nm}\ll W$ , consistent with the no-slip boundary condition observed in our experiment.

We note that a recent work ref.  $^{22}$  estimates  $\zeta \approx 500\,\mathrm{nm}$  in their system at  $T=75\,\mathrm{K}$ . With such a longer slip-length, Poiseuille flow persists because a wider channel is employed in the work, with  $W=4.7\,\mu\mathrm{m}$ . In addition,  $l_\mathrm{pp}\approx 0.16W=750\,\mathrm{nm}$ , which is much larger than in our system because of lower temperature. Hence one still has  $\zeta\approx 0.6l_\mathrm{pp}$ . In another word, the slip-length is large at lower temperature, and decreases as temperature increases.

As discussed in ref. <sup>17</sup>, a large slip-length below 100 K is consistent with the observation by the Manchester group that the Gurzhi effect is not observed up to 100 K. However, at much higher temperature, the slip-length decreases significantly; according to ref. <sup>17</sup>, the slip-length would reach a sub-100 nm value at room temperature, consistent with our experimental observation of no-slip boundary condition.

# 18 Field-dependence of viscous profiles

To check if there is significant field dependence to the observed current profiles in graphene, we performed scanning NV magnetometry at the CNP for several applied bias magnetic fields (Fig. S18). The bias field was aligned with the orientation of the NV and the values were  $B_0 = 50$ , 200, 389 G. The out-of-plane field is  $B_{0,z} = B_0/\sqrt{3} = 29$ , 115, and 225 G. At all magnetic field values, the observed current profiles maintain the overall shape for Poiseuille flow and do not have significant, qualitative change.

The corresponding cyclotron radius is  $r_C = E_{\rm F}/(ev_{\rm F}B) = 8.9$ , 2.2, and 1.1  $\mu{\rm m}$  at the three bias field values. Here, we use  $E_{\rm F} = k_{\rm B}T$ . In the regime where the cyclotron radius is larger than the width W, a hydrodynamic current profile is not expected to change<sup>22</sup>, which is consistent with our experimental observation.

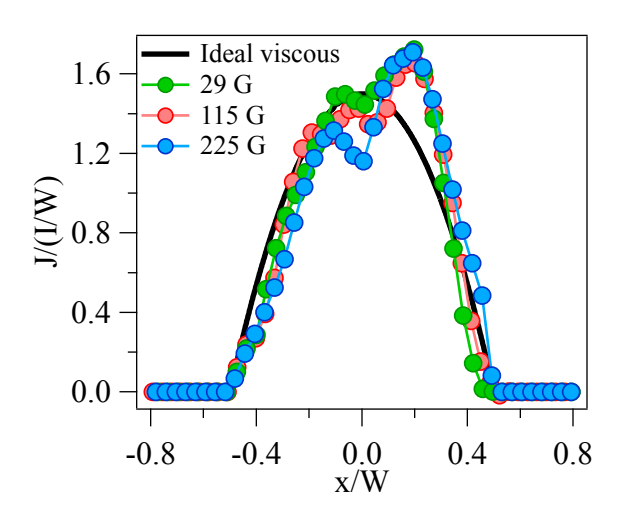


Figure S18: Current profiles at the CNP for three different out-of-plane bias magnetic fields. The current density J is normalized by average flux I/W. The x-axis is normalized by the width W. The out-of-plane field is 29 (green), 115 (red), and 225 G (blue), corresponding to cyclotron radius  $r_C=8.9, 2.2, {\rm and}\ 1.1\ \mu{\rm m}$ . Solid black curve is for ideal viscous flow.

### 19 Analysis of transport characterization of graphene device for scanning measurement

Here, we provide further analysis of the transport characterization of a graphene device studied with scanning NV magnetometry. Analysis is performed for the data shown in the middle panel of Fig. S8. The data shown in the left-most panel of Fig. S8 is almost identical, so here we only show analysis of one set of data. The data shown in the right-most panel of Fig. S8 corresponds to a device with significantly larger charge impurity; an analysis of the impurity level is shown in Section 15 of the Supplementary Information.

First, we extract the mobility  $\mu = \sigma/(en)$  from the standard formula. For  $E_{\rm F} = \hbar v_{\rm F} \sqrt{\pi n} < k_{\rm B}T$ , we use n such that  $E_{\rm F}(n) = k_{\rm B}T$ , both here and in the subsequent analysis.  $\mu$  as a function of n is shown in Fig. S19a. The benchmark of device quality is seen in the high-density regime where mobility is fairly constant. In that regime, we have  $\approx 6 \times 10^4 \, {\rm cm}^2/({\rm Vs})$ , which is on par with the  $5 \times 10^4 \, {\rm cm}^2/({\rm Vs})$  value typical for a high mobility encapsulated graphene device cited in the literature (see for example the mobility of a typical device in the Manchester group experiment<sup>8</sup>).

Next, we extract the momentum-relaxing scattering length  $l_{\rm mr}$  and viscous scattering length  $l_{\nu} \equiv \nu/v_{\rm F}$ . For  $l_{\rm mr}$ , one could apply the standard Drude formula  $l_{\rm mr} = \sigma h/(2e^2k_{\rm F})$  where the Fermi wave vector  $k_{\rm F} = \sqrt{\pi n}$ . This formula is applicable where the current profile is uniform. The resulting  $l_{\rm mr}$  is shown as black dashed curve in Fig. S19b. Given that we observed a parabolic current profile, the Drude formula will not accurately assess  $l_{\rm mr}$ . In order to assess the scattering length scales in the Poiseuille regime, we make use of the results for three values of the kinematic viscosity  $\nu$  from the main text Fig. 4b, each corresponding to a value of  $D_{\nu}/W$ .  $l_{\rm mr}$  can be obtained

from the definition of the Gurzhi length  $D_{\nu} \equiv \sqrt{l_{\rm mr}\nu/v_{\rm F}}$  and the value of  $\nu$  corresponding to each value of  $D_{\nu}/W$ .  $l_{\rm mr}$  corresponding to  $D_{\nu}/W=0.3,\ 0.5$  are shown in Fig. S19b. Note that  $l_{\rm mr}$  is not shown for  $D_{\nu}/W=\infty$  because it corresponds to  $l_{\rm mr}=\infty$ . The viscous scattering length is then given by the definition  $l_{\nu}\equiv\nu/v_{\rm F}$ , as shown in Fig. S19c.

Lastly, we show the ratio of the scattering lengths  $l_{\nu}/l_{\rm mr}$ , which is the same as  $\tau_{\nu}/\tau_{\rm mr}$ , for  $D_{\nu}/W=0.3$  (red) and 0.5 (green) in Fig. S19d. While  $\tau_{\nu}$  is not necessarily the same as  $\tau_{\rm pp}$ , they are expected to be on the same order, and hence  $\tau_{\nu}/\tau_{\rm mr}$  provides a measure to assess the validity of hydrodynamics. We found  $\tau_{\nu}/\tau_{\rm mr}$  is bounded above by 0.4 and hence significantly smaller than unity. Thus, we see that the transport measurement provides a self-consistent check that the system is in the hydrodynamic regime.

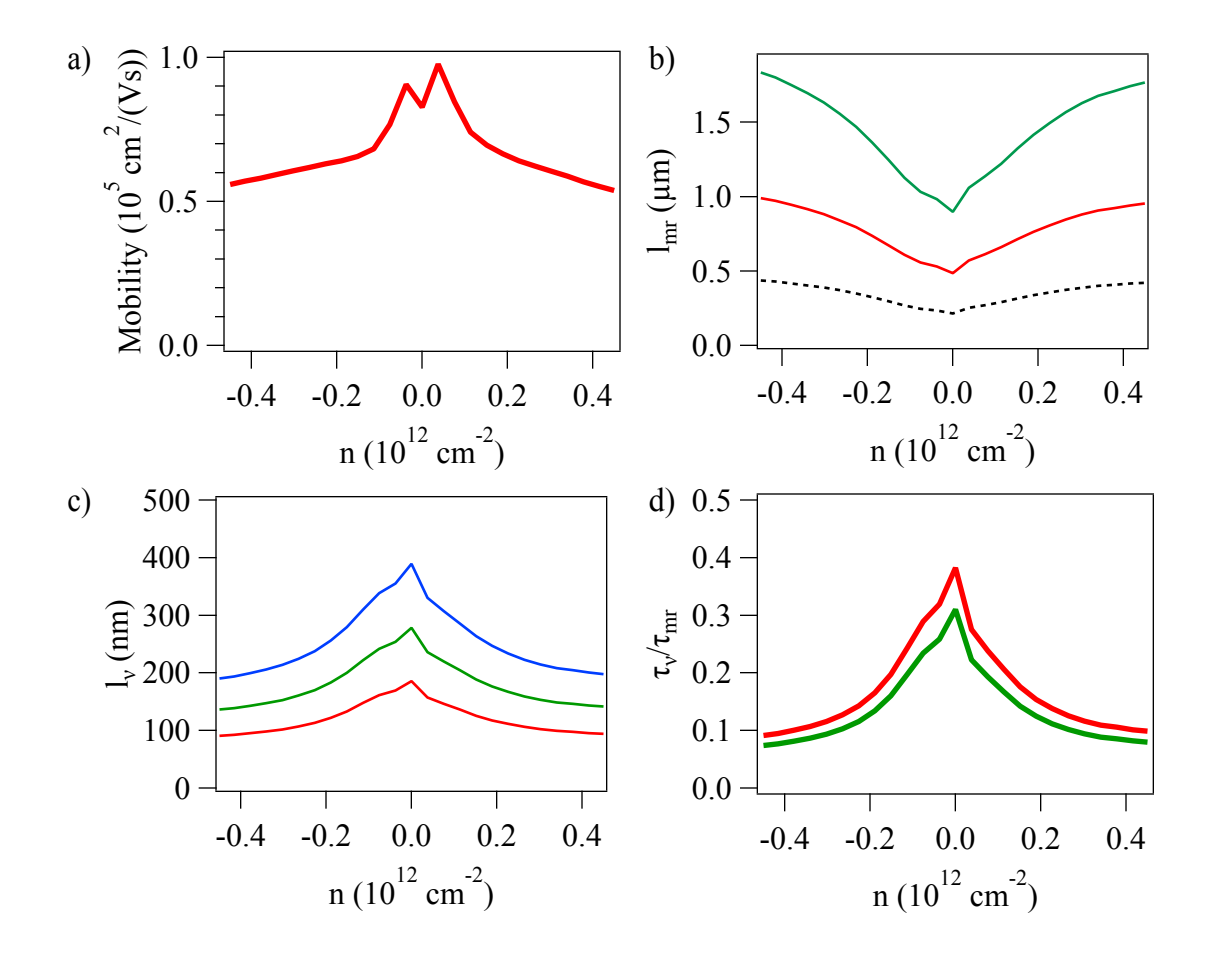


Figure S19: (a) Mobility  $\mu$  vs. carrier density n. (b) Momentum-relaxing mean free path  $l_{\rm mr}$ . Black dashed curve is the data from the Drude formula. Red and green curves are from a hydrodynamic analysis with  $D_{\nu}/W=0.3$  and 0.5. (c) Viscous scattering length  $l_{\nu}$  extracted from a hydrodynamic analysis with  $D_{\nu}/W=0.3$  (red), 0.5 (green), and  $\infty$  (blue). (d) Ratio of scattering times  $\tau_{\nu}/\tau_{\rm mr}=l_{\nu}/l_{\rm mr}$  for  $D_{\nu}/W=0.3$  (red) and 0.5 (green).

# 20 Range of channel width for Poiseuille flow in graphene at room temperature

In this section, we discuss the range of channel width W in which one may observe Poiseuille current flow in graphene at room temperature. As discussed in Supplementary Information Section 11, one expects  $D_{\nu} \approx 300-600\,\mathrm{nm}$ . Hence,  $W \lesssim 3D_{\nu} \approx 1-2\,\mu\mathrm{m}$  is the necessary regime to observe a parabolic current profile. On the other hand, W cannot be small such that the slip-length  $\zeta$  starts to become significant. Based on the work in ref. <sup>17</sup>, Supplementary Information Section 17 estimates  $\zeta \approx 80\,\mathrm{nm}$ . It is reasonable to place  $10\zeta \lesssim W$  as the criterion for Poiseuille flow. Therefore, the range in which one can expect to observe Poiseuille flow is  $0.8\,\mu\mathrm{m} \lesssim W \lesssim 2\,\mu\mathrm{m}$ .

Previous works obtained a signature of viscous Poiseuille flow in the scaling of the resistivity  $\rho \propto W^{-2}$  in a graphene point contact<sup>20</sup> and WP<sub>2</sub> (ref. <sup>23</sup>). The graphene point contact experiment covered a range of point contact width from 0.1 to 0.8  $\mu$ m, a factor of 8, while the experiment with WP<sub>2</sub> ribbon covered a range of ribbon width from 0.4 to 9  $\mu$ m, a factor of 22.5. In contrast, the range of graphene channel width at room temperature discussed above corresponds to a factor of 2.5. Hence it will be difficult to observe the resistivity scaling in the case of a graphene channel at room temperature due to the narrow range in which one has to conduct such an experiment.

# 21 Verification of continuity equation from the wide-field imaging experiment

In this section, we show line-cuts of  $J_y$  at a few different y-values, and demonstrate that the continuity equation  $\nabla \cdot \mathbf{J} = 0$  is satisfied. First, we show line-cuts  $J_y$  at several y-values in Fig S20b.  $J_y$  becomes flatter as one approaches the lower part of the channel where the current starts to bend around a corner towards the drain on the left.

In order to verify that this dynamics is real and not an imaging artifact, we probe the divergence of the current to check that the continuity equation is satisfied. In Fig. S20c, we show an example of the divergence of the current density  $\nabla \cdot \mathbf{J}$  from the wide-field imaging experiment. In the channel where we investigate Poiseuille flow, the largest value of the divergence is around  $\delta(\Delta J/\Delta x) \approx 170\mu A/\mu m^2$ . As the pixel size of the image is  $\Delta x = 0.1\mu m$ , we can provide another independent assessment of the error on the current to be  $\Delta x \delta(\Delta J/\Delta x)/2 \approx 9$  A/m. The factor of 2 in the denominator comes from error propagation in calculating the divergence, where one needs to make use of values of the current density at four points. This error estimate is consistent with the assessment from uncertainty of the stand-off distance.

We note that  $\nabla \cdot \mathbf{J}$  at the bottom-left side-probe is significantly larger compared to that in the main channel. This is due to the large magnetic gradient arising from the highly concentrated current, which leads to a distorted ODMR spectrum and inaccurate determination of the magnetic field. Due to such artifacts, one expects a much larger error in the extracted local current and hence divergence for images at this part of the device.

Next, we check that the continuity equation is satisfied in an alternative way. We can reliably obtain vertical flux  $\int \mathrm{d}x \, J_y$  in the channel above the top gate metallic contact, and we observe the flux agrees with the source-drain current  $I_{\rm sd}=100\mu\mathrm{A}$  within  $9\mu\mathrm{A}$ , which is also consistent with  $\delta J=9\mu\mathrm{A}/\mu\mathrm{m}$ . In addition, we checked that the horizontal flux  $\int \mathrm{d}y \, J_x$  at the bottom left side probe (at around  $x=-1\mu\mathrm{m}$ ) agrees with  $I_{\rm sd}$ .

Therefore, we conclude that the data is consistent with the continuity equation within the error bar. The check of the continuity equation benchmarks the reliability of our imaging technique. Given that we verify the continuity equation, we conclude that the observed spatial evolution of the current density is real and not an artifact in the measurement. Presumably, this involves higher order dynamics of the electron fluid as the current bends around the device corner, which leads the system to deviate from the equilibrium ideal Poiseuille flow in the lower part of the channel.

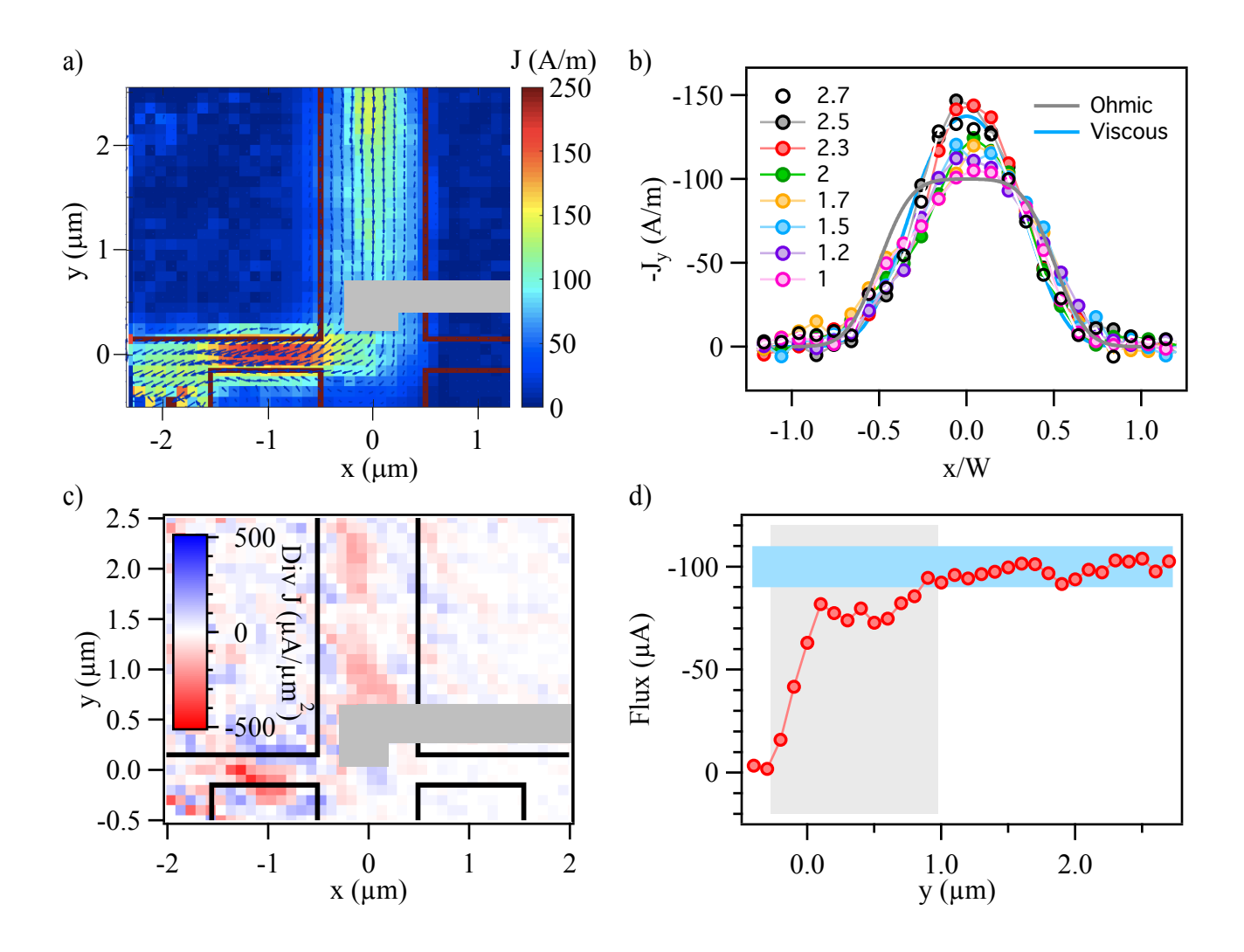


Figure S20: (a) The same image from Fig. 3b for reference. (b) Line-cuts of  $J_y$  at a few different y. The values of y (units in  $\mu$ m) corresponding to each set of data is shown in the legend. (c) Example of measured divergence of current density  $\nabla \cdot \mathbf{J}$  in graphene from wide-field imaging experiment. (d) Vertical flux  $\int \mathrm{d}x \, J_y$  as a function of y. The gray band corresponds to the region within 420 nm (imaging resolution) of the metallic top gate contact; in this region, imaging is distorted due to the presence of the contact. Blue band corresponds to  $\pm 9\,\mu\mathrm{A}$  of the source-drain current  $I_{\mathrm{sd}} = 100\,\mu\mathrm{A}$ .

### 22 Magneto-Transport Measurement

Magneto-transport measurement provides a way to determine whether transport is ballistic in graphene as a function of temperature. The measurement is performed with the hBN-encapsulated graphene device whose measured current profile is shown in Fig. 2e of the main text. An optical image of the device, together with the schematic of the transport measurement, is shown in Fig. S21a. We measure the four-terminal resistivity  $\rho$  as a function of an out-of-plane magnetic field B and carrier density n. The measurement is carried out in a Janis SVT/MAGNET cryostat. A 2D plot of the data is shown in Fig. S21b for temperature at 10 K and 270 K. At finite doping, the data for 10 K shows two prominent maxima in the resistivity, whereas the data for 270 K is largely featureless. To further highlight the difference at the two temperatures, we show line-cuts along B at several values of n. The horizontal axis is shown in units of  $W/R_C$ , where  $W=1~\mu\mathrm{m}$ is the device width and  $R_C = \hbar k_F/(eB)$  is the cyclotron radius. Here  $k_F = \sqrt{\pi n}$  is the Fermi wave vector. At 10 K, a peak in  $\rho$  occurs at  $W/R_C \approx \pm 1$ , and a kink occurs at  $W/R_C \approx \pm 2$ . These are well-known signatures of ballistic transport in graphene<sup>24,25</sup>. Hence, the device is demonstrated to exhibit ballistic transport at low temperatures, as expected for a standard hBN-encapsulated graphene device. As temperature increases, ballistic transport will disappear at some point. For our data at 270 K, the signatures of ballistic transport have disappeared. Hence we conclude that ballistic transport is no longer present at 270 K and above.

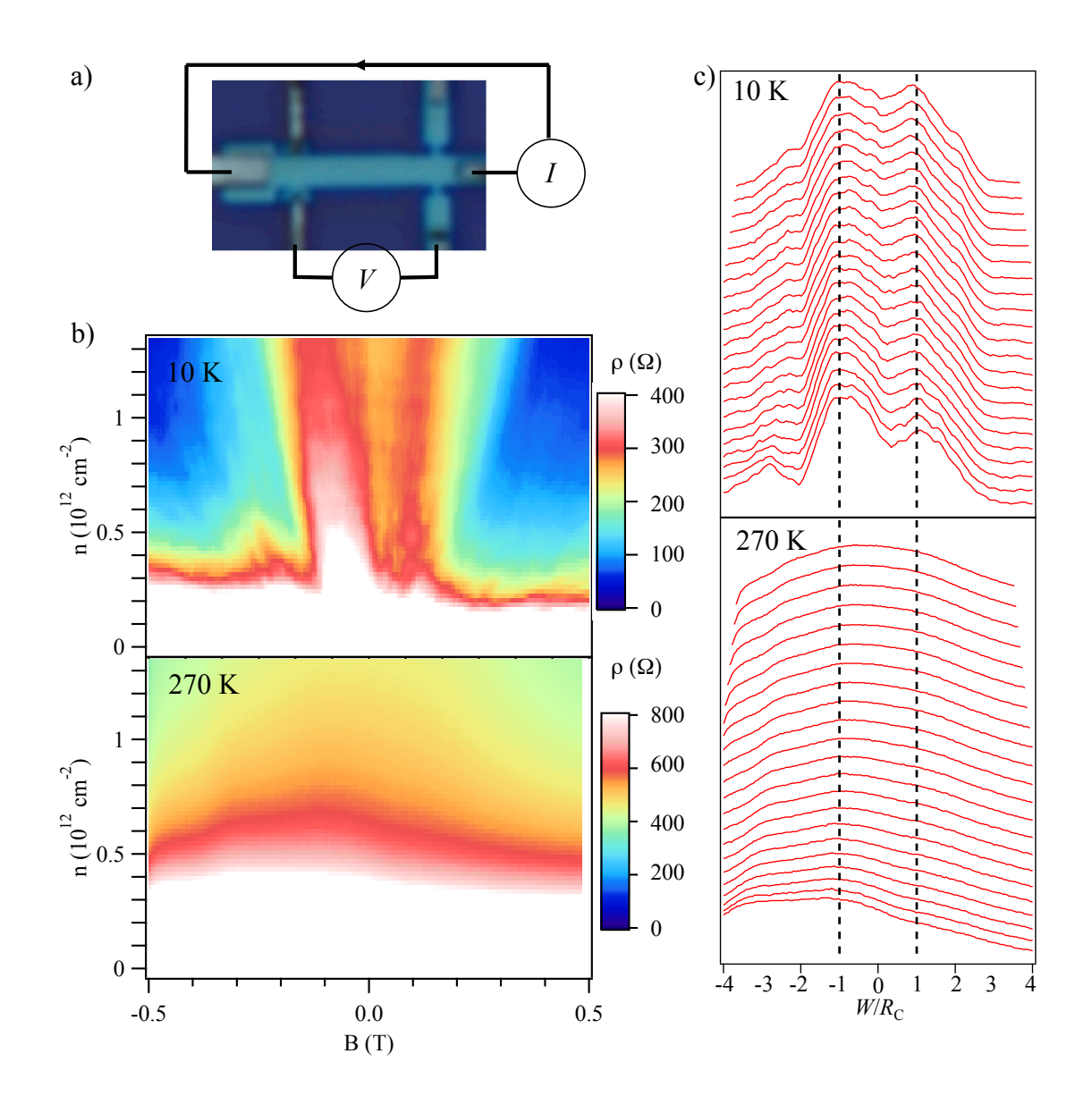


Figure S21: Magneto-transport measurements of hBN-encapsulated graphene device at 10 K and 270 K. (a) Schematic of the magneto-transport experiment, performed via measurements of the four-terminal resistivity  $\rho$ . (b) Resistivity  $\rho$  as a function of carrier density n and out-of-plane magnetic field B. The range of  $\rho$  displayed is chosen to make the relevant features visible in the colormap. At low temperature (10K), we observe a double-peak feature in  $\rho$  as B is varied. This feature is absent at 270 K. (c) 1D line-cuts of (b). The horizontal axis is shown in units of  $W/R_C$ ,

where  $W=1~\mu\mathrm{m}$  is the device width and  $R_C=\hbar k_F/(eB)$  is the cyclotron radius. Here  $k_F=\sqrt{\pi n}$  is the Fermi wave vector. Each lineaut is offset vertically. Line-cuts are shown for  $n=5.67\times 10^{11}$  to  $1.36\times 10^{12}~\mathrm{cm}^{-2}$  at  $3.78\times 10^{10}~\mathrm{cm}^{-2}$  intervals. At 10 K, a peak in  $\rho$  occurs at  $W/R_C\approx \pm 1$ , and a kink occurs at  $W/R_C\approx \pm 2$ . These features are absent at 270 K.

# 23 Current Reconstruction from Scanning NV Microscopy

Scanning NV microscopy measures only one projection of the magnetic field generated by current through the device. However, the Biot-Savart law together with continuity equation, which has the form  $k_x j_x + k_y j_y = 0$  in Fourier space, requires the map of one projection of the magnetic field to contain all information of a 2D current distribution. In our experiment, the NV has an orientation vector  $\hat{u} = (\sqrt{2/3}\cos\theta, \sqrt{2/3}\sin\theta, \sqrt{1/3})$ , where  $\theta$  is the angle between the NV orientation projected on the xy plane and the x-axis. Here, the device being studied is used to define the coordinate axis, with the long direction of the device taken as the y-direction. Therefore, the projected field is  $B_{||}(x) = \sqrt{2/3}\cos\theta B_x(x) + \sqrt{1/3}B_z(x)$ . The sample is placed on the setup in such a way as to minimize  $\theta$ .

There are two challenges with applying the Fourier inversion method described previously to scanning measurements. First,  $B_{||}$  involves  $B_z$ , which has a long  $\sim 1/x$  tail. Direct inversion requires measurement over a large field of view or otherwise leads to long-wavelength artifacts (e.g., offsets or a slope), which in general can be corrected but nevertheless are inconvenient. Second, current reconstruction involves inverting a low-pass filter which, in the absence of other low-pass filter such as optical diffraction, leads to amplification of noise at high frequencies. Therefore, regularization is required<sup>26</sup>. However, regularization needs to be performed with care: a naive application of a global regularization can smoothen out a sharp feature, such as at the edges.

The goal is to have a current reconstruction procedure that is generally applicable to an

arbitrary current profile  $J_y(x)$  flowing in a channel oriented along the y-direction. First, the current density is parameterized as  $J_y=J_y(\{a_n\},x)$ , with  $\{a_n\}$  being free parameters that determine  $J_y$ . It is convenient to capture the expected overall shape of the current profile with a minimal number of parameters in a function called  $J_0$ . For this purpose, the functional form of Eq. 1 of the main text is chosen, which can vary from a parabola to a rectangular function. While  $J_0$  is the solution of the electronic Navier Stoke equation, it is used here merely to set the functional form without assuming hydrodynamics. The second part of the parameterization  $\Delta J$  captures the remaining variation; it is a linear interpolation with N equally spaced points inside the channel and parametrized by the values  $a_n=\Delta J(x_n)$ , where  $x_n\equiv -\frac{W}{2}+n\frac{W}{N}$  for n=0,1,...,N is the  $n^{\rm th}$  equally-spaced point along the width of the channel. Since the behavior at the edges is already captured by  $J_0$ , it is allowed to set  $a_0,a_N=0$ . The mathematical expression for the parameterization is

$$J_y(x, W, D, \{a_n\}) = A_0 J_0(x, W, D) + \Delta J(x, W, N, \{a_n\}),$$
 (S25)

$$J_0(x, W, D) \equiv \left(1 - \frac{\cosh(x/D)}{\cosh(W/(2D))}\right) \Pi(x/W), \qquad (S26)$$

$$\Delta J(x, W, N, \{a_n\}) \equiv \sum_{n=1}^{N} J_{\text{lin}}(x - (x_{n-1} + x_n)/2, W/N, a_{n-1}, a_n), \qquad (S27)$$

$$J_{\text{lin}}(x, \Delta W, a, b) \equiv \left( \left( \frac{b-a}{\Delta W} \right) x + \frac{a+b}{2} \right) \Pi(x/\Delta W).$$
 (S28)

Here,  $\Pi(x)$  is the rectangular function, which is unity for |x| < 1/2 and zero otherwise. Note that no particular model is assumed for the current density; also the parameterization described above allows  $J_y$  to take on any functional form. The only prior knowledge exploited in this procedure is the fact that the current density is zero outside the channel.

With this parameterization, functional can be constructed that generates  $B_{||}$  for a given  $J_y$ :

$$B_{\parallel}(x, x_{\text{ctr}}, W, D, \{a_n\}, d, \theta, B_0) = B_0 + \sqrt{\frac{2}{3}} \cos(\theta) \alpha_x(x, d) * J_y(x - x_{\text{ctr}}, W, D, \{a_n\}) + \frac{1}{\sqrt{3}} \alpha_z(x, d) * J_y(x - x_{\text{ctr}}, W, D, \{a_n\}).$$
 (S29)

Here,  $x_{\text{ctr}}$  is the center of the channel, d is the stand-off distance,  $B_0$  is an offset that accounts for potential contribution in  $B_z$  from far away current flowing not strictly in the y-direction, \* denotes a 1D convolution, and the kernels are

$$\alpha_x(x,d) \equiv \frac{\mu_0}{2\pi} \frac{d}{(d^2 + x^2)} \tag{S30}$$

$$\alpha_z(x,d) \equiv -\frac{\mu_0}{2\pi} \frac{x}{(d^2 + x^2)}.$$
 (S31)

To obtain the parameters  $\{x_{\text{ctr}}, W, D, \{a_n\}, d, \theta, B_0\}$ , the cost function is minimized:

$$\chi^2 = \sum_{i} |B_{||}(x_i, x_{\text{ctr}}, W, D, \{a_n\}, d, \theta, B_0) - B_{||,i}|^2,$$
(S32)

where  $\{x_i, B_{||,i}\}$  is the experimental data.

Inverting the Biot-Savart law, which acts as a low-pass filter, without regularization leads to unphysical amplification of high-frequency noises on the magnetic field, and therefore regularization is routinely required for the inverse problem. Here, regularization is performed by subjecting the  $\chi^2$  minimization to a global constraint  $|\Delta J''| < \Delta J''_{\rm max}$ , where  $\Delta J''$  is the (numerical) second derivative of  $\Delta J$ . This is equivalent to a low-pass filter of the form  $k^{-2}$  in Fourier space. The constraint  $\Delta J''_{\rm max}$  is chosen such that the reduced  $\chi^2$  is close to unity,  $\chi^2_{\nu} \equiv \chi^2/[\delta B^2(N_{\rm d}-N_{\rm p})] \approx 1$ . Here,  $\delta B$  is the typical error bar of the data,  $N_{\rm d}$  is the number of data points and  $N_{\rm p}$  are the number of free parameters in the functional. We note that  $J_0$  itself is well-behaved, and therefore only regularization on  $\Delta J$  is necessary.

# 24 Comparison of imaging techniques

In this section, we provide a summary of different imaging techniques for probing electronic transport in graphene<sup>22,27–32</sup> and discuss their utility in the context of imaging hydrodynamic current flow. The table below provides a summary of the key specifications for each technique. The most critical requirement is the ability to operate above 100 K, which is the temperature range of hydrodynamic current flow in graphene. This requirement excludes Josephson junction, SQUID, and scanning gate microscopy. Note that scanning gate microscopy has been applied to probe electron hydrodynamic in a 2D electron gas<sup>31</sup>, where hydrodynamics is observed at a much lower temperature compared to graphene.

Graphene current imaging technique	Temperature of operation	Spatial resolution	Quantity measured	References
Single NV scanning probe	<600 K; this work 300K	~50 nm	B-field (projective)	This work
Josephson junction	10 mK	~200 nm	Supercurrent	Allen <i>et al.</i> Nat. Phys. <b>12</b> , 128 (2015)
Ensemble NV wide field imaging	<600 K; this work 300K	420 nm	B-field (vector)	This work, Tetienne <i>et al.</i> Sci. Adv. <b>3</b> , e1602429 (2017).
Nano SQUID	<4.2 K	~50 nm	$B$ -field ( $B_z$ )	Uri et al. Nat. Phys. 16, 164 (2020).
Scanning gate microscopy	<4.2K	~50 nm*, ~200 nm#	Perturbation on current from scanning gate	*Aidala <i>et al.</i> Nat. Phys. <b>3</b> , 464 (2007), #Braem <i>et al.</i> Phys. Rev. B <b>98</b> , 241304(R) (2018)
Scanning SET	<300K	880 nm	E-field	Ella <i>et al.</i> Nat. Nanotechnol. <b>14</b> , 480 (2019), Sulpizio <i>et al.</i> Nature <b>576</b> , 75 (2019).

- 1. Roth, B. J., Sepulveda, N. G. & Wikswo Jr, J. P. Using a magnetometer to image a two-dimensional current distribution. *Journal of Applied Physics* **65**, 361–372 (1989).
- 2. Pham, L. M. *et al.* NMR technique for determining the depth of shallow nitrogen-vacancy centers in diamond. *Physical Review B* **93**, 045425 (2016).
- Toyli, D. M., Weis, C. D., Fuchs, G. D., Schenkel, T. & Awschalom, D. D. Chip-scale nanofabrication of single spins and spin arrays in diamond. *Nano Letters* 10, 3168–3172 (2010).
- 4. Levitov, L. & Falkovich, G. Electron viscosity, current vortices and negative nonlocal resistance in graphene. *Nature Physics* **12**, 672 (2016).
- 5. Beenakker, C. W. J. & van Houten, H. Boundary scattering and weak localization of electrons in a magnetic field. *Physical Review B* **38**, 3232–3240 (1988).
- 6. Wang, L. *et al.* One-dimensional electrical contact to a two-dimensional material. *Science* **342**, 614–617 (2013).
- 7. Li, Q. & Das Sarma, S. Finite temperature inelastic mean free path and quasiparticle lifetime in graphene. *Physical Review B* **87**, 085406 (2013).
- 8. Bandurin, D. A. *et al.* Negative local resistance caused by viscous electron backflow in graphene. *Science* **351**, 1055–1058 (2016).
- 9. Ju, L. *et al.* Photoinduced doping in heterostructures of graphene and boron nitride. *Nature Nanotechnology* **9**, 348 (2014).

- 10. Neumann, C. *et al.* Spatial control of laser-induced doping profiles in graphene on hexagonal boron nitride. *ACS Applied Materials & Interfaces* **8**, 9377–9383 (2016).
- 11. Chandni, U., Watanabe, K., Taniguchi, T. & Eisenstein, J. P. Evidence for defect-mediated tunneling in hexagonal boron nitride-based junctions. *Nano Letters* **15**, 7329–7333 (2015).
- 12. Cadore, A. R. *et al.* Thermally activated hysteresis in high quality graphene/h-BN devices. *Applied Physics Letters* **108**, 233101 (2016).
- 13. Joucken, F. *et al.* Visualizing the effect of an electrostatic gate with angle-resolved photoemission spectroscopy. *Nano Letters* **19**, 2682–2687 (2019).
- 14. Xue, J. *et al.* Scanning tunnelling microscopy and spectroscopy of ultra-flat graphene on hexagonal boron nitride. *Nature Materials* **10**, 282 (2011).
- 15. Shivaprasad, S. M., Udachan, L. A. & Angadi, M. A. Electrical resistivity of thin palladium films. *Physics Letters A* **78**, 187–188 (1980).
- 16. Vargas, W. E. Optical, magnetic, and charge-carriers transport properties of a transition metal: bulk palladium. *Applied Optics* **56**, 6496–6503 (2017).
- 17. Kiselev, E. I. & Schmalian, J. Boundary conditions of viscous electron flow. *Physical Review B* **99**, 035430 (2019).
- 18. Bandurin, D. A. et al. Fluidity onset in graphene. Nature Communications 9, 4533 (2018).
- 19. Berdyugin, A. I. *et al.* Measuring Hall viscosity of graphenes electron fluid. *Science* **364**, 162 (2019).

- 20. Krishna Kumar, R. *et al.* Superballistic flow of viscous electron fluid through graphene constrictions. *Nature Physics* **13**, 1182 (2017).
- 21. Gallagher, P. *et al.* Quantum-critical conductivity of the Dirac fluid in graphene. *Science* **364**, 158 (2019).
- 22. Sulpizio, J. A. *et al.* Visualizing Poiseuille flow of hydrodynamic electrons. *Nature* **576**, 75–79 (2019).
- 23. Gooth, J. *et al.* Thermal and electrical signatures of a hydrodynamic electron fluid in tungsten diphosphide. *Nature Communications* **9**, 4093 (2018).
- 24. Masubuchi, S. *et al.* Boundary scattering in ballistic graphene. *Physical Review Letters* **109**, 036601 (2012).
- 25. Scaffidi, T., Nandi, N., Schmidt, B., Mackenzie, A. P. & Moore, J. E. Hydrodynamic electron flow and hall viscosity. *Physical Review Letters* **118**, 226601 (2017).
- 26. Meltzer, A. Y., Levin, E. & Zeldov, E. Direct reconstruction of two-dimensional currents in thin films from magnetic-field measurements. *Physical Review Applied* **8**, 064030 (2017).
- 27. Allen, M. T. *et al.* Spatially resolved edge currents and guided-wave electronic states in graphene. *Nature Physics* **12**, 128 (2015).
- 28. Tetienne, J.-P. *et al.* Quantum imaging of current flow in graphene. *Science Advances* 3, e1602429 (2017).

- 29. Uri, A. *et al.* Nanoscale imaging of equilibrium quantum Hall edge currents and of the magnetic monopole response in graphene. *Nature Physics* **16**, 164–170 (2020).
- 30. Aidala, K. E. *et al.* Imaging magnetic focusing of coherent electron waves. *Nature Physics* **3**, 464 (2007).
- 31. Braem, B. A. *et al.* Scanning gate microscopy in a viscous electron fluid. *Physical Review B* **98**, 241304(R) (2018).
- 32. Ella, L. *et al.* Simultaneous voltage and current density imaging of flowing electrons in two dimensions. *Nature Nanotechnology* **14**, 480–487 (2019).